Abstract

Aircraft icing continues to be a threat for modern day aircraft. Icing occurs when supercooled large droplets (SLD's) impinge on the body of the aircraft. These droplets can bounce off, freeze on impact or freeze partly with the remaining liquid running further down the body. This results in different ice shapes.
Several different computer programs have been developed to predict these ice shapes. An example of such a program is 2DFOIL-ICE. 2DFOIL-ICE calculates droplet trajectories using the Lagrangian method. It also calculates the stationary flow around the two-dimensional airfoil to determine different aerodynamic coefficients.
To compare the modeled results of the two-dimensional wing to a three-dimensional wing, a modeled ice shape has been fabricated on an ATR-72 wing. To determine the effects of icing on this wing, the wing with icing will be tested in a wind tunnel and compared to a clean ATR-72 wing. These results will then be compared to the results from 2DFOIL to determine the accuracy of the numerical method.

Table of Contents

List of symbols

Latin symbols

Symbol	Property	Unit
A	Axial force	[N]
A	Area	[m^2]
a	Local speed of sound	[m·s^{-1}]
$\vec{a}$	Acceleration	[m·s^2]
c	Chord length	[m]
C_D	Three-dimensional drag coefficient	-
c_d	Two-dimensional drag coefficient	-
C_L	Three-dimensional lift coefficient	-
c_l	Two-dimensional lift coefficient	-
C_M	Three-dimensional moment coefficient	-
c_m	Two-dimensional moment coefficient	-
D	Drag force	[N]
e	Internal energy	[J]
f	Number of degrees of freedom	-
F	Force	[N]
g	Gravitational constant	[m·s^{-2}]
k	Thermal conductivity constant	[J·s^{-1}·m^{-1}·K^{-1}]
L	Lift force	[N]
M	Moment	[Nm]
m	Mass	[kg]
M_∞	Mach number	-
N	Normal force	[N]
p	Pressure	[N·m^{-2}]
$\dot{q}$	Heat flux	[J·s^{-1}·m^{-2}]
q_∞	Free-stream dynamic pressure	[N·m^{-2}]
R	Molar gas constant	[J·mol^{-1}·K^{-1}]
R'	Resultant aerodynamic force	[N]
Re	Reynolds number	-
S	Planform area	[m^2]
T	Temperature	[K]
u	x-component of the velocity	[m·s^{-1}]
v	y-component of the velocity	[m·s^{-1}]
V	Velocity	[m·s^{-1}]
w	z-component of the velocity	[m·s^{-1}]

Greek symbols

Symbol	Property	Unit
α	Angle of attack	[rad]
γ	Adiabatic index	-
ε	Strain	-
λ	Bulk viscosity coefficient	[$N \cdot s \cdot m^{-2}$]
μ	Viscosity	[$N \cdot s \cdot m^{-2}$]
μ_∞	Dynamic viscosity	[$N \cdot s \cdot m^{-2}$]
ρ	Density	[$kg \cdot m^{-3}$]
τ	Shear stress	[$N \cdot m^{-2}$]
Φ	Velocity potential	-

Subscripts

Symbol	Property
$_{LE}$	Leading edge
$_{TE}$	Trailing edge
$_{c/4}$	Quarter chord length
$_\infty$	Free-stream

1 Aircraft icing

1.1 Introduction

Icing conditions are a hazard for modern day airliners and continue to be an important field of research. A recent incident that involved icing was with a Russian Boeing 747-8F. The aircraft, cruising at an altitude of approximately 12500 meters, flew into a cloud full of undetectable ice crystals that caused significant damage to three of the four engines. The aircraft managed to land safely, but one of the four engines experienced a speed reduction of 70% (Norris, 2013).

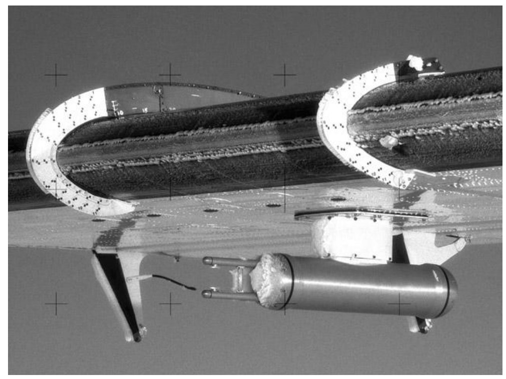

Figure 1.1 In-flight image of ice accretion on a wing during flight of NASA's Twin Otter icing research aircraft (NASA Icing Branch, 2014)

Icing occurs when a supercooled water droplet or ice crystal hits the aircraft, flying in an environment where the temperature is at or below the freezing point of water. Droplets are a more severe hazard, as they stick more easily to the aircraft surface than ice crystals. As the droplets hit the wings or fuselage of the aircraft, they can freeze and cause non-aerodynamic shapes. These shapes can reduce aerodynamic properties like the drag or lift of the aircraft. Icing can also occur on the nacelles, propellers or engine intake. Icing in these regions can cause engine failure, because ice formed in these regions can suddenly let loose and seriously damage the inside of the engine (Hospers & Hoeijmakers, 2010).

1.2 Icing regimes

When a supercooled droplet impinges on the wing, it can do two things. It fully freezes upon impact, or it partially freezes and runs further down the wing. This leads to two different sorts of ice accretion. Rime ice is created when the droplet fully freezes upon impact and glaze ice is formed when the droplet partially freezes and runs down the wing. A mixture of these two forms of ice can also occur.

Figure 1.2 Rime ice

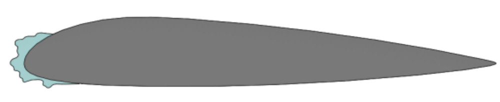

Figure 1.3 Glaze ice

Rime ice results in a more streamlined ice shape (Figure 1.2). It occurs in temperature ranges from -10°C to -20°C and at low airspeeds. Air can be trapped in the ice because of the quick freezing process. Because of this, the density of rime ice is lower than the density of water. Rime ice has a white, brittle appearance.

Glaze ice results in an irregular, non-aerodynamic shape (Figure 1.3). It occurs in temperature ranges between -5°C and the freezing point of water and at high airspeeds. Because the temperature is close to the freezing point and latent heat is released during the freezing process, the temperature can rise above the freezing point. This means the droplet partially freezes and runs down the wing. Glaze ice has a clear, solid appearance (Norde, 2013).

1.3 ATR-72 wing

The wing used in the wind tunnel experiments is an ATR-72 wing. This wing is used on the ATR 72-500 aircraft, which is a propeller aircraft that can carry approximately 70 people (ATR aircraft products, ATR 72-500 series). The real wing has a span of 27.05 meters and an area of 61.00 m^2. The wing to be tested in the wind tunnel has a span of 0.455 m. The wing on the ATR 72-500 has no sweep.

At 31 October 1994, an accident occurred in the United States at Roselawn, IN, in which an ATR-72-212 aircraft was involved. The plane encountered a cloud containing supercooled droplets. This resulted in the formation of a ridge of ice beyond the de-ice boots located on the wings of the aircraft. This ridge of ice caused a sudden and unexpected aileron hinge moment reversal, after which the plane lost control and crashed. All of the passengers and crew deceased (Aviation Safety Network).

2 Aerodynamics

2.1 Introduction

To understand the phenomena involving winged bodies moving through a fluid, some knowledge about aerodynamics is needed. All aerodynamic properties needed to perform the experiments in this report are in this chapter.

2.2 Aerodynamic forces and moments

Figure 2.1 represents a winged body moving through a fluid. A fluid can be either a gas or a liquid. The two basic sources of aerodynamic forces on a body are the pressure distribution and shear stress distribution over the body surface. The pressure (*p*) acts normal to the surface, whereas the shear stress (τ) acts perpendicular to the surface. The body can be divided into an upper and lower part, where s_u is the distance from the leading edge measured along the body surface to an arbitrary point A on the upper surface. Similarly, s_l is the distance from the leading edge to an arbitrary point B on the lower surface (Figure 2.2).

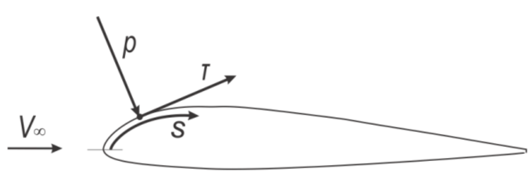

Figure 2.1 Winged body in free-stream

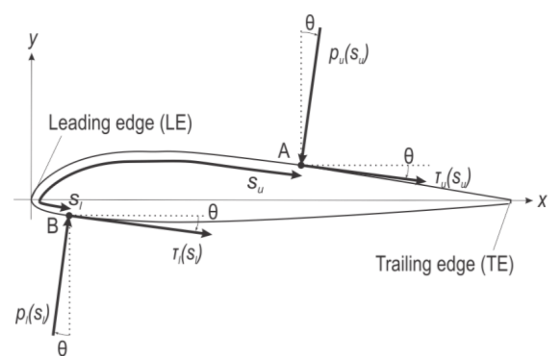

Figure 2.2 Winged body, divided into upper and lower part, in a Cartesian coordinate system

Integrating the pressure and shear stress distribution over the distance along the upper and lower surface results in a resultant aerodynamic force (*R'*) and moment (*M*). *R* can be split into an axial force (*A*) and a normal force *(N)* (Figure 2.4).

The total normal and axial forces can be determined by integrating the pressure and shear stress distribution along the body surface.

$$N' = \int_{LE}^{TE} (p_u \cos\theta + \tau_u \sin\theta)\, ds_u + \int_{LE}^{TE} (p_l \cos\theta - \tau_l \sin\theta)\, ds_l \quad (2.1)$$

$$A' = \int_{LE}^{TE} (-p_u \sin\theta + \tau_u \cos\theta)\, ds_u + \int_{LE}^{TE} (p_l \sin\theta + \tau_l \cos\theta)\, ds_l \quad (2.2)$$

Where θ is the angle between the pressure and shear stress and the local coordinate system. In both equations the first term is the integral over the upper surface and the second term is the integral over the lower surface.

The axial and normal forces are not dependent on the angle of attack (α). The angle of attack is defined as the angle between the chord (c) and the free-stream velocity (V_∞). Free-stream is defined as the flow far away from the body. *R'* can be split into the lift (L) and drag *(D)* (Figure 2.4). The lift and drag force are important because the lift force is always perpendicular to the free-stream and the drag force always parallel, independent on the angle of attack.

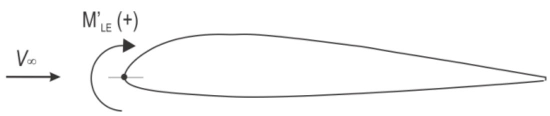

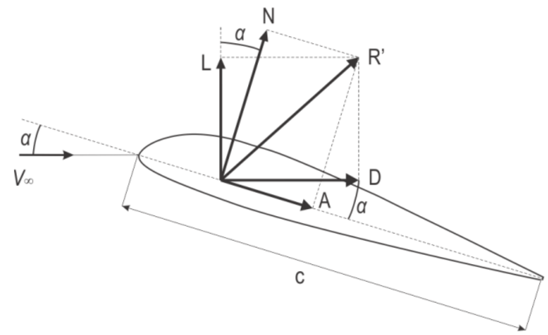

Figure 2.3 Free body diagram of a winged body in free-stream, with angle of attack α

Figure 2.4 Moment about the leading edge

The normal and axial forces can be rewritten to the lift and drag.

$$L = N\cos\alpha - A\sin\alpha \tag{2.3}$$

$$D = N\sin\alpha + A\cos\alpha \tag{2.4}$$

The moment about the leading edge (Figure 2.3) is obtained by using the same method as used in Equation (2.1) and (2.2). By convention, moments that tend to increase α are positive and moments that tend to decrease α are negative (Figure 2.3). The moment about the trailing edge per unit span is given by:

$$M'_{LE} = \int_{LE}^{TE}[(p_u\cos\theta + \tau_u\sin\theta)x + (-p_u\sin\theta + \tau_u\cos\theta)y]\,ds_u$$
$$+\int_{LE}^{TE}[(-p_l\cos\theta + \tau_l\sin\theta)x \ + (p_l\sin\theta + \tau_l\cos\theta)y]\ ds_l \tag{2.5}$$

Where *x, y* and θ are known functions of *s* for a given body shape (Figure 2.2). The lift, drag and moment about the leading edge can be expressed as dimensionless coefficients. To achieve this, a quantity called the free-stream dynamic pressure (q_∞) has to be introduced. This dynamic pressure will be explained in chapter 3.3.2.

$$q_\infty \equiv \frac{1}{2}\rho_\infty V_\infty^2 \tag{2.6}$$

Where ρ_∞ and V_∞ are the density and velocity, respectively, in free-stream. q_∞ is given in force per meter square. The lift coefficient (C_l), drag coefficient (C_d) and moment coefficient (C_m) can now be defined.

$$C_L \equiv \frac{L}{q_\infty S} \tag{2.7}$$

$$C_D \equiv \frac{D}{q_\infty S} \tag{2.8}$$

$$C_M \equiv \frac{M}{q_\infty Sc} \tag{2.9}$$

Where *S* is the planform area of the wing and *c* the chord length. The coefficients given in Equations (2.7), (2.8) and (2.9) are written in capital letters, which denotes coefficients for a complete three-dimensional body. *L, D* and *M* denote the forces and moment that act on the entire three-dimensional wings. The coefficients for a two-dimensional airfoil are written in lower-case letters and are given in Equations (2.10), (2.11) and (2.12).

$$c_l \equiv \frac{L\prime}{q_\infty c} \tag{2.10}$$

$$c_d \equiv \frac{D\prime}{q_\infty c} \tag{2.11}$$

$$c_m \equiv \frac{M\prime}{q_\infty c^2} \tag{2.12}$$

Note that the planform area *S* is given by $c \cdot 1$, which gives the coefficients in unit span^{-1}. The coefficients for an airfoil can be calculated using numerical techniques. The coefficients for a three-dimensional wing are usually determined by experiment, for instance in a wind tunnel.

2.3 Reynolds and Mach number

Because wind tunnel experiments are usually performed at small dimensions, two dimensionless quantities will be introduced to be able to compare these flow results to different flow situations. These dimensionless quantities are the Reynolds number and Mach number. These numbers are given by the following equations:

$$Re = \frac{\rho_\infty V_\infty c}{\mu_\infty} \tag{2.13}$$

$$M_\infty = \frac{V_\infty}{a} \tag{2.14}$$

Where *Re* is the Reynolds number, ρ_∞ the density, V_∞ the free-stream velocity, *c* the chord length, μ_∞ the dynamic viscosity, M_∞ the mach number and *a* the local speed of sound. The local speed of sound can be expressed as:

$$a = \sqrt{\gamma RT} \tag{2.15}$$

Where γ is the adiabatic index, *R* is the molar gas constant and *T* is the temperature. The adiabatic index is given by:

$$\gamma = 1 + \frac{2}{f} \tag{2.16}$$

Where f is the number of degrees of freedom of the molecules in the gas. Because air consists mostly of diatomic molecules, which have 5 degrees of freedom, γ will be 1.4.

2.4 Bernoulli's theorem

An important equation in fluid dynamics is Bernoulli's equation. It relates the pressure to the velocity at different points along a streamline. Bernoulli's principle states:

$$p + \frac{1}{2}\rho V^2 = constant\ along\ streamlines \tag{2.17}$$

Equation (2.17) is valid as long as the flow is steady, inviscid and incompressible. If these conditions are met, Bernoulli's principle holds along a streamline for a rotational flow and holds at every point throughout an irrotational flow. Body forces such as gravity are neglected. Bernoulli's principle can be applied on a contraction section, which is used in a wind tunnel. This contraction section has two cross-sectional areas. Rewriting Equation (2.17) yields the formula for the pressure drop over these two areas.

$$P_1 + \frac{1}{2}\rho V_1^2 = P_2 + \frac{1}{2}\rho V_2^2 \tag{2.18}$$

$$\Delta P = \frac{1}{2}\rho(V_1^2 - V_2^2) \tag{2.19}$$

Where V_1 and P_1 are the velocity and pressure at cross-section A_1 and V_2 and P_2 are the velocity and pressure at cross-section A_2.

The quasi-one-dimensional continuity equation for incompressible flow relates V_1 and V_2 to A_1 and A_2.

$$A_1 V_1 = A_2 V_2 \tag{2.20}$$

$$V_1 = A_2 V_2 / A_1 \tag{2.21}$$

Combining Equations (3.10) and (3.12) gives:

$$\Delta P = \frac{1}{2}\rho((A_2/A_1)^2 V_2^2 - V_2^2) = \frac{1}{2}\rho V_2^2((A_2/A_1)^2 - 1) \tag{2.22}$$

2.5 Downwash

The coefficients for an airfoil (Equations (2.10) to (2.12)) usually differ from the coefficients for a three-dimensional wing (Equations (2.7) to (2.9)). The reason for this difference is because three-dimensional bodies also have a flow that is three-dimensional, which means there is a flow component in the spanwise direction. This flow is caused by the difference in pressure between the upper and lower side of the wing and causes tip vortices. These tip vortices induce a small velocity component in the downward direction at the wing. This effect is called downwash and is elaborated in Figure 2.5.

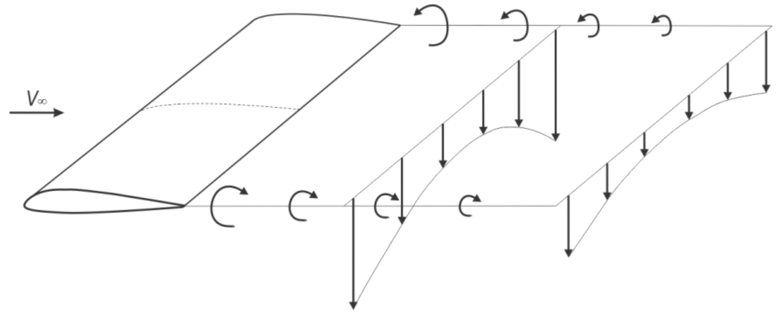

Figure 2.5 Induced downwash as a result of tip vortices

2.6 Navier-Stokes equations

To be able to model the forces on the airfoils, some information about the flow field surrounding the airfoil is needed. An important set of equations to describe the motion of viscous fluids, is the Navier-Stokes equations. These equations arise from applying Newton's second law to fluid motion. Newton's second law states:

$$\vec{F} = m\vec{a} \tag{2.23}$$

Where $\vec{F}$ is the force acting on an object, m is the mass of this object and $\vec{a}$ is the acceleration.

An infinitesimally small, moving fluid element of fixed mass is adopted to model the flow. Each face of the fluid element experiences tangential and normal stresses and the surrounding pressure. These stresses are displayed in Figure 2.6.

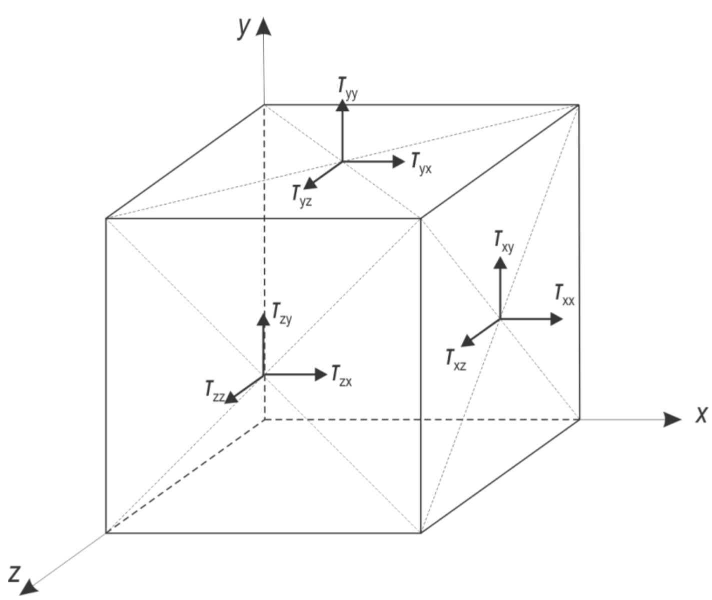

Figure 2.6 Tangential and normal stresses acting on an infinitesimally small, moving fluid element

$\vec{F}$ is the sum of all the body and surface forces acting on this fluid element. In vector notation, Equation (2.23) becomes:

$$\begin{pmatrix} F_x \\ F_y \\ F_z \end{pmatrix} = m \begin{pmatrix} a_x \\ a_y \\ a_z \end{pmatrix} \tag{2.24}$$

F_x is the sum of the forces in the x-direction due to the pressure and all stresses in the x-direction. All forces in the x-direction are displayed in Figure 2.7.

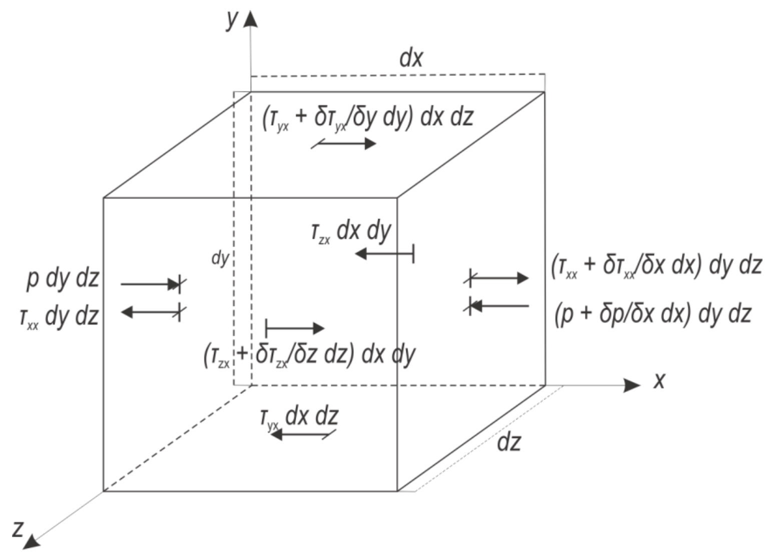

Figure 2.7 Forces and pressures in the x-direction on an infinitesimally small, moving fluid element

Adding all forces results in the net force in the x-direction acting on the fluid element. Note that forces pointing to the right are positive and forces pointing to the left are negative.

$$F_x = \left[p - \left(p + \frac{\partial p}{dx}dx\right)\right] dy\, dz + \left[\left(\tau_{xx} + \frac{\partial \tau_{xx}}{\partial x}dx\right) - \tau_{xx}\right] dy\, dz + \left[\left(\tau_{yx} + \frac{\partial \tau_{yx}}{\partial y}dy\right) - \tau_{yx}\right] dx\, dz + \left[\left(\tau_{zx} + \frac{\partial \tau_{zx}}{\partial z}dz\right) - \tau_{zx}\right] dx\, dy \tag{2.25}$$

Which can be simplified to:

$$F_x = \left(-\frac{\partial p}{dx} + \frac{\partial \tau_{xx}}{\partial x} + \frac{\partial \tau_{yx}}{\partial y} + \frac{\partial \tau_{zx}}{\partial z}\right) dx\, dy\, dz = m \cdot a_x \tag{2.26}$$

The acceleration vector can be written as:

$$\begin{pmatrix} a_x \\ a_y \\ a_z \end{pmatrix} = \begin{pmatrix} \frac{Du}{Dt} \\ \frac{Dv}{Dt} \\ \frac{Dw}{Dt} \end{pmatrix} \tag{2.27}$$

Here, *u*, *v* and *w* are the velocities in x, y, and z direction, respectively. The *D/Dt* terms indicates a substantial derivative. The substantial derivative indicates the time rate of change of a given fluid element as it moves through space. As u is a function of x, y, z and t, the substantial derivative of u can be written as:

$$\frac{Du}{Dt} = \frac{\partial u}{\partial x} + \frac{\partial u}{\partial y} + \frac{\partial u}{dz} + \frac{\partial u}{\partial t} \tag{2.28}$$

The mass of the infinitesimally small, moving fluid element is simply the density times the volume of the fluid element.

$$m = \rho \, dx \, dy \, dz \tag{2.29}$$

Combining Equations (2.26), (2.27) and (2.29) gives:

$$\rho \frac{Du}{Dt} = -\frac{\partial p}{dx} + \frac{\partial \tau_{xx}}{\partial x} + \frac{\partial \tau_{yx}}{\partial y} + \frac{\partial \tau_{zx}}{\partial z} \tag{2.30}$$

Which is the momentum equation in the x-direction. Applying the same method for the y- and z-direction gives the momentum equations in y- and z-direction.

$$\rho \frac{Dv}{Dt} = -\frac{\partial p}{dy} + \frac{\partial \tau_{xy}}{\partial x} + \frac{\partial \tau_{yy}}{\partial y} + \frac{\partial \tau_{zy}}{\partial z} \tag{2.31}$$

$$\rho \frac{Dw}{Dt} = -\frac{\partial p}{dw} + \frac{\partial \tau_{xz}}{\partial x} + \frac{\partial \tau_{yz}}{\partial y} + \frac{\partial \tau_{zz}}{\partial z} \tag{2.32}$$

Equations (2.30) through (2.32) are scalar equations called the Navier-Stokes equations. These equations can be elaborated further by creating an expression for the different stresses (Figure 2.6). In fluid dynamics, stress is related to the time rate of strain by the proportionality constant μ, which is the viscosity of the fluid. The two-dimensional time rate of strain is given by the following formulas:

$$\varepsilon_{xy} = \frac{\delta v}{\delta x} + \frac{\delta u}{dy} \tag{2.33}$$

$$\varepsilon_{xz} = \frac{\delta w}{\delta x} + \frac{\delta u}{dz} \tag{2.34}$$

$$\varepsilon_{yz} = \frac{\delta w}{\delta y} + \frac{\delta v}{dz} \tag{2.35}$$

By looking at Figure 2.6 it becomes clear that ε_{xy} must be caused by tangential stresses τ_{xy} and τ_{yx}. The same applies for the strain in the xz- and yz-plane. Multiplying Equation (2.33) to (2.35) with the viscosity gives the formulas for the tangential stresses.

$$\tau_{xy} = \tau_{yx} = \mu \left(\frac{\delta v}{\delta x} + \frac{\delta u}{dy} \right) \tag{2.36}$$

$$\tau_{xz} = \tau_{zx} = \mu \left(\frac{\delta w}{\delta x} + \frac{\delta u}{dz} \right) \tag{2.37}$$

$$\tau_{yz} = \tau_{yz} = \mu \left(\frac{\delta w}{\delta y} + \frac{\delta v}{dz} \right) \tag{2.38}$$

The normal stresses displayed in Figure 2.7 act to compress or expand the fluid element. The normal stresses can be expressed as:

$$\tau_{xx} = \lambda\left(\nabla \cdot \vec{V}\right) + 2\mu\frac{\delta u}{dx} \tag{2.39}$$

$$\tau_{yy} = \lambda\left(\nabla \cdot \vec{V}\right) + 2\mu\frac{\delta v}{dy} \tag{2.40}$$

$$\tau_{zz} = \lambda\left(\nabla \cdot \vec{V}\right) + 2\mu\frac{\delta w}{dz} \tag{2.41}$$

Where $\nabla \cdot \vec{V}$ is the dilatation of the fluid element and λ is the bulk viscosity coefficient. Equations (2.30) through (2.32) can now be combined with Equations (2.36) through (2.41) to create the complete Navier-Stokes equations for an unsteady, compressible, three-dimensional viscous flow.

$$\rho\left(u\frac{\partial u}{\partial x} + v\frac{\partial u}{\partial y} + w\frac{\partial u}{dz} + \frac{\partial u}{\partial t}\right) = -\frac{\partial p}{dx} + \frac{\partial}{\partial x}\left(\lambda\left(\nabla \cdot \vec{V}\right) + 2\mu\frac{\delta u}{dx}\right) + \frac{\partial}{\partial y}\left(\mu\left(\frac{\delta v}{\delta x} + \frac{\delta u}{dy}\right)\right) + \frac{\partial}{\partial z}\left(\mu\left(\frac{\delta w}{\delta x} + \frac{\delta u}{dz}\right)\right) \tag{2.42}$$

$$\rho\left(u\frac{\partial v}{\partial x} + v\frac{\partial v}{\partial y} + w\frac{\partial v}{dz} + \frac{\partial v}{\partial t}\right) = -\frac{\partial p}{dy} + \frac{\partial}{\partial x}\left(\mu\left(\frac{\delta v}{\delta x} + \frac{\delta u}{dy}\right)\right) + \frac{\partial}{\partial y}\left(\left(\nabla \cdot \vec{V}\right) + 2\mu\frac{\delta v}{dy}\right) + \frac{\partial}{\partial z}\left(\mu\left(\frac{\delta w}{\delta y} + \frac{\delta v}{dz}\right)\right) \tag{2.43}$$

$$\rho\left(u\frac{\partial w}{\partial x} + v\frac{\partial w}{\partial y} + w\frac{\partial w}{dz} + \frac{\partial w}{\partial t}\right) = -\frac{\partial p}{dz} + \frac{\partial}{\partial x}\left(\mu\left(\frac{\delta w}{\delta x} + \frac{\delta u}{dz}\right)\right) + \frac{\partial}{\partial y}\left(\mu\left(\frac{\delta w}{\delta y} + \frac{\delta v}{dz}\right)\right) + \frac{\partial}{\partial z}\left(\lambda\left(\nabla \cdot \vec{V}\right) + 2\mu\frac{\delta w}{dz}\right) \tag{2.44}$$

For incompressible, viscous flow the momentum and continuity equations are sufficient, but for compressible flow an additional equation is needed, namely the energy equation. For this energy equation, the same infinitesimally small fluid element as used for the previous Navier-Stokes equations is used. The first law of thermodynamics can be applied to this fluid element. Expressed in terms of *A*, *B* and *C*, this gives:

$$A = B + C \tag{2.45}$$

Where A is the rate of change of the energy inside the fluid element, B is the net flux of heat into the element and C is the rate of work done on the element due to pressure and stress forces on the surface of the element. The rate of work done on the fluid element can be obtained by multiplying the forces and pressures displayed in Figure 2.7 with the velocity component in the x-direction. Adding the heat flux results in Figure 2.8.

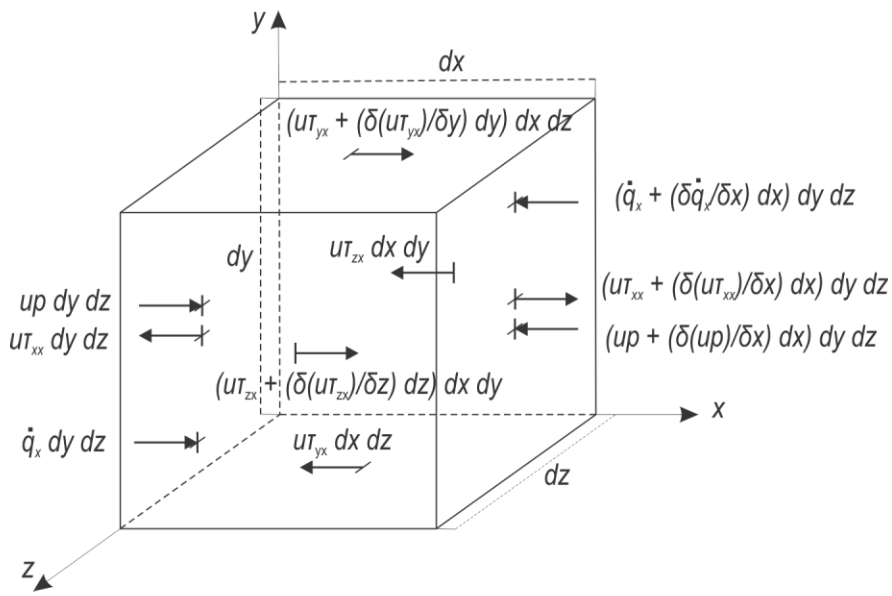

Figure 2.8 Rate of work and heat flux in the x-direction on an infinitesimally small, moving fluid element

The total rate of work in the x-direction can be expressed as:

$$\left(-\frac{\partial(up)}{\partial x}+\frac{\partial(u\tau_{xx})}{\partial x}+\frac{\partial(u\tau_{yx})}{\partial y}+\frac{\partial(u\tau_{zx})}{\partial z}\right)dx\,dy\,dz \tag{2.46}$$

The total rate of work in the y- and z- direction can be determined with the same approach as in the x-direction. This results in the three-dimensional equation of the rate of work on an infinitesimally small fluid element:

$$C=\left(-\left(\frac{\partial(up)}{\partial x}+\frac{\partial(vp)}{\partial y}+\frac{\partial(wp)}{\partial z}\right)+\frac{\partial(u\tau_{xx})}{\partial x}+\frac{\partial(u\tau_{yx})}{\partial y}+\frac{\partial(u\tau_{zx})}{\partial z}+\frac{\partial(v\tau_{xy})}{\partial x}+\frac{\partial(v\tau_{yy})}{\partial y}+\frac{\partial(v\tau_{zy})}{\partial z}+\frac{\partial(w\tau_{xz})}{\partial x}+\frac{\partial(w\tau_{yz})}{\partial y}+\frac{\partial(w\tau_{zz})}{\partial z}\right)dx\,dy\,dz \tag{2.47}$$

Where *v* is the velocity in the y direction and *w* is the velocity in the z direction. The same can be done for the heat of the fluid element by thermal conduction. Taking all three dimensions into account, the following expression is obtained:

$$Heating\ of\ fluid\ element\ by\ thermal\ conduction=-\left(\frac{\partial\dot{q}_x}{\partial x}+\frac{\partial\dot{q}_y}{\partial y}+\frac{\partial\dot{q}_z}{\partial z}\right)dx\,dy\,dz \tag{2.48}$$

The volumetric heating of the fluid element can be expressed as:

$$Volumetric\ heating\ of\ element=\rho\dot{q}\,dx\,dy\,dz \tag{2.49}$$

Where ρ is the density of the fluid element. The term $\dot{q_x}$ can be written as:

$$\dot{q_x}=-k\frac{\partial T}{\partial x} \tag{2.50}$$

Where *k* is the thermal conductivity constant and *T* is the temperature. Combining Equations (2.38) to (2.40) results in the net flux of heat into the element *B.*

$$B = \left(\rho\dot{q} + \frac{\partial}{\partial x}\left(k\frac{\partial T}{\partial x}\right) + \frac{\partial}{\partial y}\left(k\frac{\partial T}{\partial y}\right) + \frac{\partial}{\partial z}\left(k\frac{\partial T}{\partial z}\right)\right) dx\, dy\, dz \tag{2.51}$$

The rate of change of energy inside the fluid element *A* can be described as:

$$A = \rho\frac{D}{Dt}\left(e + \frac{V^2}{2}\right) dx\, dy\, dz \tag{2.52}$$

Where the term $\rho\, dx\, dy\, dz$ is the mass of the element and *e* is the internal energy. $\frac{V^2}{2}$ stands for the kinetic energy of the fluid element, where *V* is the velocity. $\frac{D}{Dt}$ is the substantial derivative. Combining *A, B,* and *C* now gives the final form of the energy equation for a viscous flow.

$$\rho\frac{D(e+V^2/2)}{Dt} = \rho\dot{q} + \frac{\partial}{\partial x}\left(k\frac{\partial T}{\partial x}\right) + \frac{\partial}{\partial y}\left(k\frac{\partial T}{\partial y}\right) + \frac{\partial}{\partial z}\left(k\frac{\partial T}{\partial z}\right) - \nabla\cdot p\vec{V} + \frac{\partial(u\tau_{xx})}{\partial x} + \frac{\partial(u\tau_{yx})}{\partial y} + \frac{\partial(u\tau_{zx})}{\partial z} + \frac{\partial(v\tau_{xy})}{\partial x} + \frac{\partial(v\tau_{yy})}{\partial y} + \frac{\partial(v\tau_{zy})}{\partial z} + \frac{\partial(w\tau_{xz})}{\partial x} + \frac{\partial(w\tau_{yz})}{\partial y} + \frac{\partial(w\tau_{zz})}{\partial z} \tag{2.53}$$

Equation (2.53) is the general energy equation for unsteady, compressible, three-dimensional, viscous flow.

2.7 Potential flow theory

If the fluid elements in the stream of the airfoil have a motion through space that is a pure translation and the fluid elements have no angular velocity, the flow is called irrotational. This implies that:

$$\nabla \times \vec{V} = 0 \tag{2.54}$$

Where $\vec{V}$ is the velocity vector. The continuity equation for incompressible flow states that:

$$\nabla \cdot \vec{V} = 0 \tag{2.55}$$

Combining Equations (2.54) and (2.55), together with the vector identity given in Equation (2.56) results in the Laplace equation for the velocity potential (Equation (2.57)).

$$\nabla \times (\nabla\phi) = 0 \tag{2.56}$$

$$\nabla^2\phi = 0 \tag{2.57}$$

Where ϕ is a scalar function. Using this scalar function results in a great simplification. Instead of dealing with three velocity components, the velocity potential can be dealt with as one unknown. The x-, y- and z- component of the velocity can be determined by Equation (2.58) to (2.60).

$$u = \frac{\partial \phi}{dx} \tag{2.58}$$

$$v = \frac{\partial \phi}{dy} \tag{2.59}$$

$$w = \frac{\partial \phi}{dz} \tag{2.60}$$

2.8 Boundary layer theory

If the flow over an airfoil is considered viscous, which is the case in a wing moving through an airflow, the viscosity and thermal conduction of the flow are important factors. To determine the effects of viscosity, an airflow over a solid surface is considered. A frictional force will arise as a result of the friction between the surface and the flow over the surface, called the skin friction. This force per unit area is defined as the shear stress (τ) and has an effect on the velocity profile close to the surface. The velocity of the flow will reduce as it gets closer to the body surface and will be zero at the body surface (Figure 2.9).

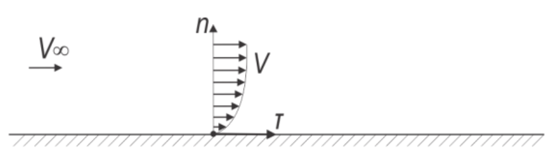

Figure 2.9 Velocity profile over a viscous flow over a solid surface

If the flat, solid surface is replaced by an airfoil, there will be an increase in the static pressure as the flow moves further down the airfoil. This increase in static pressure follows from Bernoulli's equation (chapter 2.4) and is called an adverse pressure gradient. The combination of this adverse pressure gradient and the effects of skin friction may eventually result in a reversed flow, especially at high angles of attack (Figure 2.10).

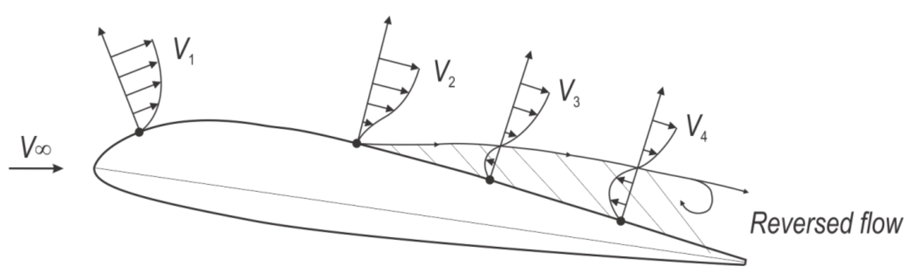

Figure 2.10 Velocity profile over a viscous flow over an airfoil, resulting in a reversed flow

This reversed flow causes the flow to separate. In Figure 2.10, this separation point occurs at the surface of velocity profile V_2. This flow separation causes a large wake of recirculating flow further down the airfoil. The wake results in a pressure drag due to flow separation. The drag due to viscosity on the airfoil can be divided into the skin friction drag D_f, which is the integral of the shear stress τ over the airfoil, and the pressure drag D_p, which is the drag due to flow separation. If the flow is smooth and regular, as in free-stream, the flow is called laminar. If the flow is uneven and irregular, as in the reversed flow region in Figure 2.10, the flow is called turbulent.

There will be a point in the velocity profile at which the velocity is equal to the free-stream velocity. This will occur at a height above the airfoil called δ, which is the velocity boundary layer thickness. The boundary layer is the region close to the body surface where the effects of viscosity are significant, which causes the flow to be retarded because of friction between the solid surface and the fluid. The boundary layer thickness can be more precisely defined as the point at which:

$$u(y) = 0.99\, u_e, \text{ with } u_e = V_\infty \tag{2.61}$$

Where *u(y)* is the velocity profile at a distance *y* above the body surface and u_e is the velocity at the outer edge of the velocity boundary layer. Another quantity that will change above the body surface is the temperature. Again, the temperature boundary layer thickness δ_T is the point at which

$$T(y) = 0.99\, T_e, \text{ with } T_e = T_\infty \tag{2.62}$$

Where *T(y)* is the temperature profile at a distance *y* above the body surface and T_e is the temperature at the outer edge of the velocity boundary layer. The boundary layer thickness experiences an increase as the flow experiences a transition from laminar to turbulent (Figure 2.11).

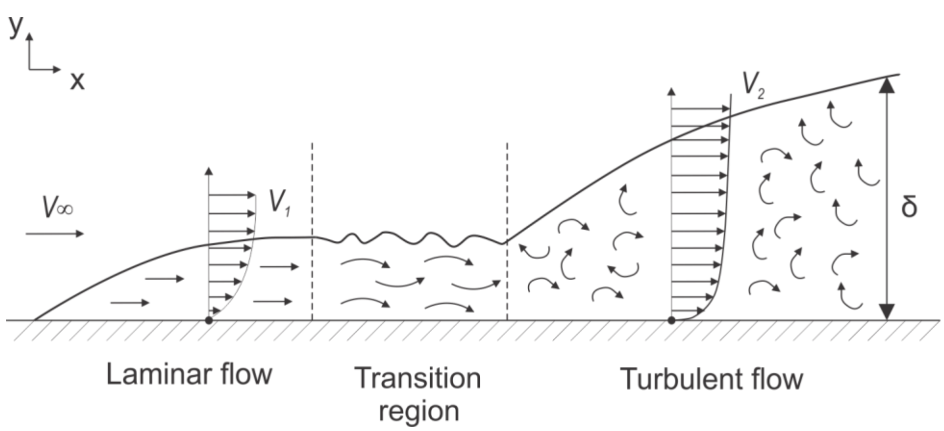

Figure 2.11 Boundary layer on the flow over a body surface

3 Wind tunnel testing

3.1 Introduction

A wind tunnel is a useful tool to measure the aerodynamic properties of a wing. A wind tunnel can be either open or closed. A closed wind tunnel has a closed circuit through which the air flows, whereas the air in an open wind tunnel exits through an exit nozzle. The difference between these two is that closed wind tunnels can usually achieve a higher free-stream velocity.

A steady flow with constant free-stream velocity is created in the test section. The model is mounted on a force balance, which can measure the lift, drag and pitching moment over a range of angles of attack. The lift-, drag- and moment coefficients can be determined from this lift- and drag force and moment, which can then be plotted versus the angle of attack. In this case, an ATR-72 wing without ice accretion is compared to an ATR-72 wing with glaze ice accretion.

3.2 Experimental set-up

A cross-sectional view of the measurement setup is shown in Figure 3.1. The wind tunnel used in this case is an open wind tunnel. It is powered by a fan that creates an airflow (part 1). The airflow that leaves part one is turbulent. To create a laminar flow in the test section (part 3), the velocity of the airflow is reduced by the widening in part 2. The shape of the narrowing in part 2 increases the velocity of the airflow again in such a way that the flow stays laminar. The flow then enters the test section (part 3) steady and laminar. The flow exits through the nozzle in part 4. The nozzle is not used in this case. This wind tunnel has a maximum velocity of approximately 25 m/s.

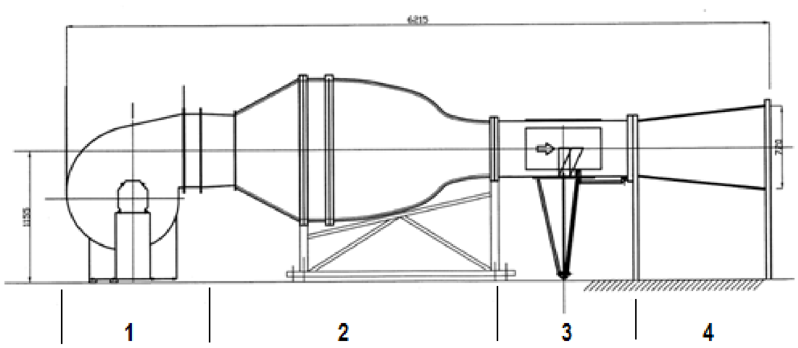

Figure 3.1 Cross-sectional view of a free-stream open wind tunnel

In this experiment, the ATR-72 wing consists of a rear end, a clean front end and a front end with a glaze ice profile. These parts can be combined to create a clean wing (Figure 3.2) and a wing with icing (Figure 3.3).

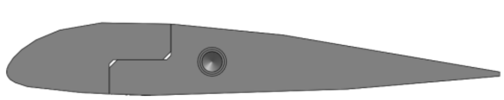

Figure 3.2 Clean wing, side view

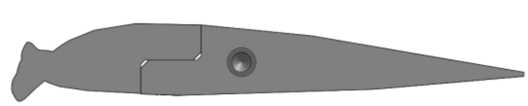

Figure 3.3 Wing with icing, side view

The test section has a cross-sectional area of 0.458 m by 0.458 m. Because the wing has a span of 0.455 m, there is only a small gap of 1.5 mm between the wing and the wall of the test section. The result of this is that the three-dimensional effects on the wing tips, as explained in chapter 2.3, can be neglected and the wing can be considered two-dimensional. The length of the test section is 1.225 m. The wing is mounted vertically in the test section (Figure 3.4) on a plateau with an adjustable angle of attack. The fixing points are located at the top and bottom of the test section. The force meter is connected on the bottom of the test section. The wing is mounted on the pitching axis. The dimensions of both wings are displayed in Figures 3.5 and 3.6.

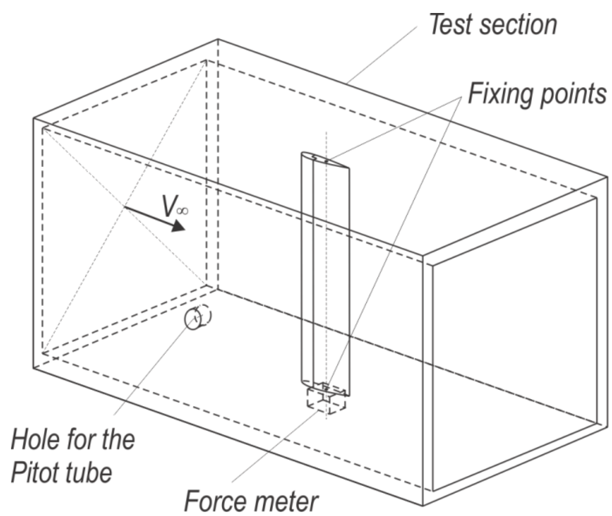

Figure 3.4 Location of the wing, force meter and Pitot tube hole in the test section of the wind tunnel

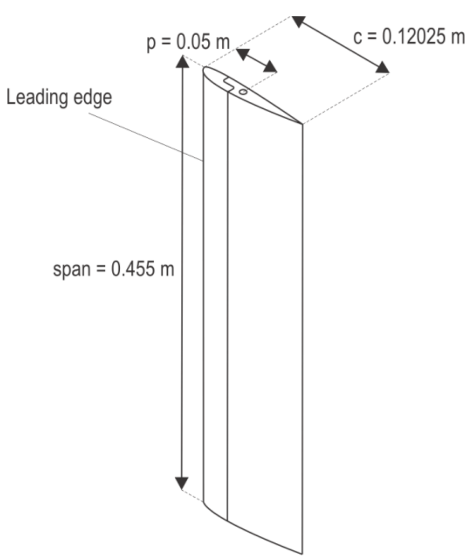

Figure 3.5 Dimensions of the clean wing

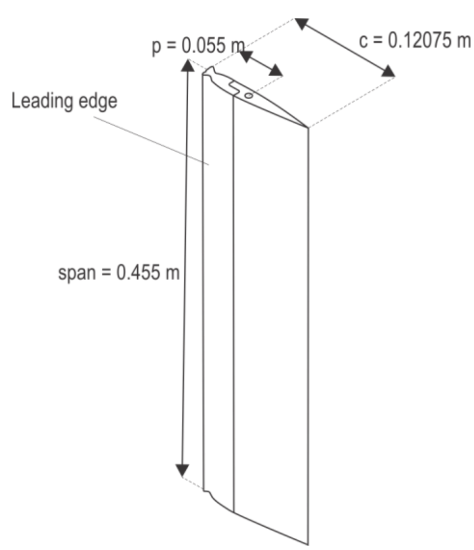

Figure 3.6 Dimensions of the wing with icing

3.3 Measurements

Different quantities have to be determined before the actual testing of the wings can commence. These quantities include the ambient pressure and the free-stream velocity. The output of the force meter can be transformed to the axial force *A*, normal force *N* and pitching moment *M* by using a correlation matrix.

3.3.1 Ambient pressure

The ambient pressure can be determined by using a barometer. The barometer gives the ambient pressure in mmHg. This pressure has to be converted from mmHg to Pa. The following formulas are used:

$$F = m \cdot a \tag{3.1}$$

$$P = \frac{F}{A} \tag{3.2}$$

Where *F* is the force on an object and *P* is the pressure. A dimensional analysis of Equations (3.1) and (3.2) shows that the pressure in Pa is correct.

$$F = [kg][m][s]^{-2} \tag{3.3}$$

$$P = [kg][m][s]^{-2}[m]^{-2} = [kg][m]^{-1}[s]^{-2} \tag{3.4}$$

$$g = [m][s]^{-2} \tag{3.5}$$

$$\rho = [kg][m]^{-3} \tag{3.6}$$

Where *g* is the gravitational constant and *ρ* is the density. Combining Equation (3.4), (3.5) and (3.6) with the height of the mercury in the barometer located near the wind tunnel results in the formula for the ambient pressure in Pa.

$$P_{ambient} = \rho_{mercury} \cdot g \cdot h_{mercury} \tag{3.7}$$

Where $\rho_{mercury}$ is the density of mercury and $h_{mercury}$ is the height of the mercury in the barometer.

3.3.2 Free-stream velocity

The free-stream velocity in the test section can be determined by using a Pitot tube (Figure 3.7). The Pitot tube is an L-shaped device with an opening at the end normal to the flow (part 1 in Figure 3.7) and small openings perpendicular to the flow at the wall of the Pitot tube (part 2 in Figure 3.7). The openings perpendicular to the flow measure the static pressure (P_∞) in the stream. The static pressure is a measure of purely the random motion of the gas. It is the pressure experienced when moving at the local velocity of the gas. The hole that is normal to the flow will experience a higher pressure than the holes perpendicular to the flow because the free-stream velocity will cause the gas particles to rush into the hole and eventually stagnate. The pressure built up in the Pitot tube caused by this velocity is called the dynamic pressure (q_∞). These two sections are connected to a manometer that measures the difference between the dynamic and static pressure in terms of a difference in height of the manometer fluid. The digital Pitot tube used in this case already displays the dynamic pressure in Pa. Measurements with the Pitot tube have to be performed in the test section without a wing, because the Pitot tube will disturb the free-stream. The Pitot tube is brought into the free-stream through a hole in the side of the test section (Figure 3.4).

The free-stream velocity can be determined by relating the dynamic pressure measured by the Pitot tube with the pressure drop over the contraction section measured by a manometer (Figure 3.8). The relation between the pressure drop and dynamic pressure follows from Bernoulli's principle (chapter 2.4).

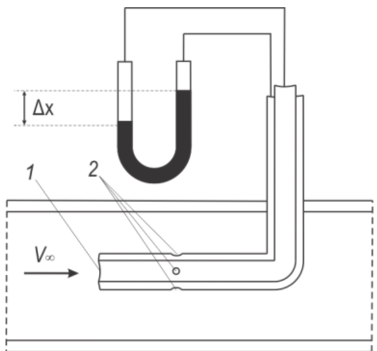

Figure 3.7 Schematic view of a Pitot tube

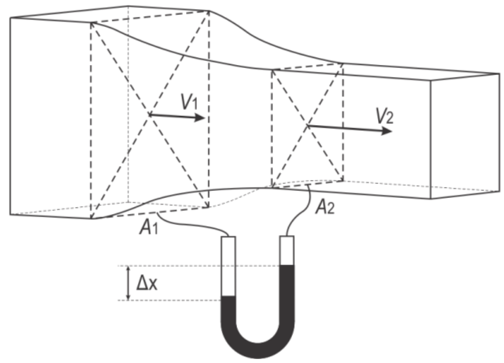

Figure 3.8 Schematic view of the contraction in the wind tunnel, with fixed taps at cross-sections A_1 and A_2 connected to a manometer

The dynamic pressure measured by the Pitot tube in the test section is given by:

$$q_\infty = \frac{1}{2}\rho V_2^2 \tag{3.8}$$

$$V_2^2 = 2q_\infty/\rho \tag{3.9}$$

The density can be determined by using the ideal gas law.

$$PV = nRT \tag{3.10}$$

$$\rho = \frac{P_{ambient}}{R \cdot T_{flow}} \tag{3.11}$$

Where T_{flow} is the temperature of the air flow in the test section. This temperature can be measured using a temperature probe.

A relation between the pressure drop in the contraction section and the dynamic pressure can now be described as:

$$\Delta P = q_\infty((A_2/A_1)^2 - 1) \tag{3.12}$$

By determining the desired free-stream velocity in the test section, the required dynamic pressure can be calculated using Equation (3.8). This dynamic pressure is related to the pressure drop measured by the manometer through Equation (3.12).

3.3.3 Lift, drag and moment coefficient

The axial force (*A*) and normal force (*N*) and pitching moment (*M*) are calculated using the output of the force meter and correlation matrix. The three-dimensional lift coefficient (C_L) and drag coefficient (C_D) can be calculated using Equations (2.7) and (2.8). The moment calculated by the force meter is the moment around the fixing point of the wing. This moment has to be rewritten to the moment around a quarter chord length (Figure 3.9).

$$M_{c/4} = M + \left(\frac{c}{4} - x_f\right) N \tag{3.13}$$

Where *M* is the moment around the fixing point of the wing, c is the chord length and x_f is the distance from the leading edge to the fixing point of the wing.

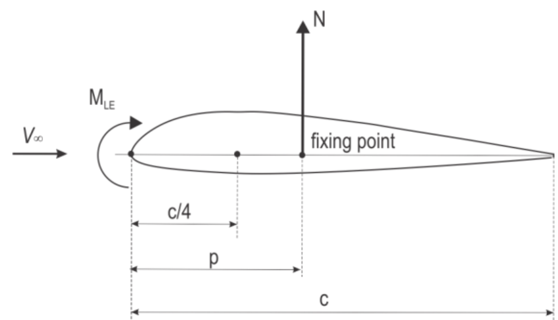

Figure 3.9 Airfoil with necessary dimensions

The moment coefficient about a quarter chord length now becomes:

$$C_{M,c/4} = \frac{M_{c/4}}{q_\infty \cdot c \cdot S} \tag{3.14}$$

3.3.4 Calibration

The force meter has to be calibrated before the measurements can commence. The force meter consists of three strain gauges that measure the axial and normal force and moment about the pitching axis in terms of a voltage drop. This voltage drop can be related to the force in Newtons by applying a known force or moment on the wing. The known force in this case is a load of ten kilograms. The calibration is done in three steps. The axial force is calibrated by applying a load tangential to the chord of the wing. The normal force is calibrated by applying a load perpendicular to the chord of the wing. The point on which the force acts is in line with the fixing point of the wing. The moment is calibrated by applying a moment of 10 Nm on the fixing point of the wing. A bar is mounted on the axis on which the wing is mounted. This bar can rotate around the fixing point of the wing. A load of 10 N is then connected to this bar to apply a moment of 10 Nm. The calibration setup is shown in Figure 3.10 to 3.12. When the calibration is done, a correlation matrix can be created to translate the measured voltage drops into the required forces and the required moment.

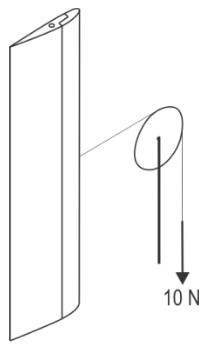

Figure 3.10 Calibration of *A*

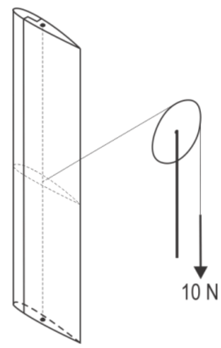

Figure 3.11 Calibration of *N*

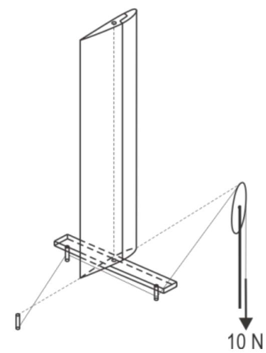

Figure 3.12 Calibration of M_{pitch}

3.4 Results

Both the clean wing and the wing with ice have been measured at the highest possible velocity of the wind tunnel. Measurements have been performed at every 1°, in a range of angles of attack from -20° to 20°. Also, between -4° and 4°, measurements were done every 0.5°. The high velocity was chosen because the force meter in the wind tunnel becomes more precise at higher velocities. The dimensions used in all calculations are the dimensions given in Figure 3.5. The obtained data can be found in Appendix C.

	T_{flow} (K)	**Density** (kg/m^3)	**Ambient pressure** (Pa)	**ΔP** (Pa)	**Dynamic pressure** (Pa)	**Free-stream velocity** (m/s)	**Reynolds number**	**Mach number**
Clean wing	295.25	1.19	100475	386	374	25.12	$2.005 \cdot 10^5$	0.0792
Wing with icing	295.35	1.19	100475	386	374	25.12	$2.005 \cdot 10^5$	0.0792

Table 3.1 Measured and calculated values used in the wind tunnel experiments

The aerodynamic coefficients can be calculated using Equations (2.7), (2.8) and (3.20). The resulting coefficient curves are given in Figure 3.13 to 3.17.

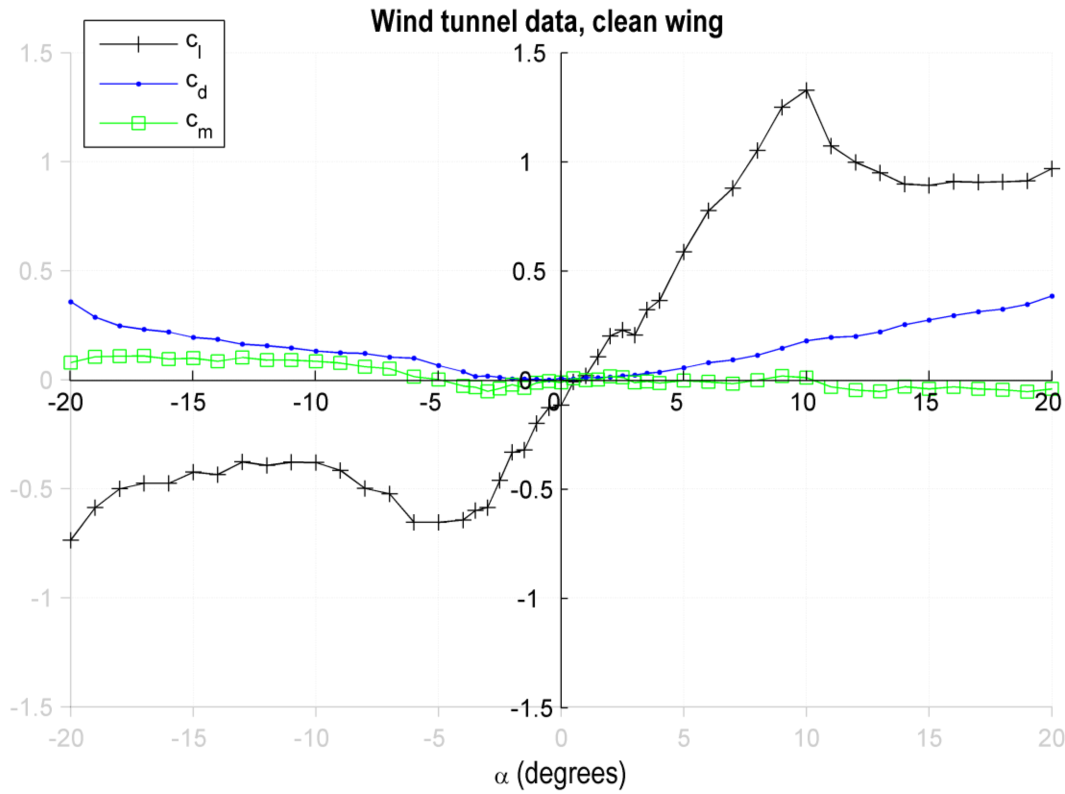

Figure 3.13 c_l, c_d, and c_m plotted versus α for a clean wing. Re = $2.005 \cdot 10^5$, M_∞ = 0.0792

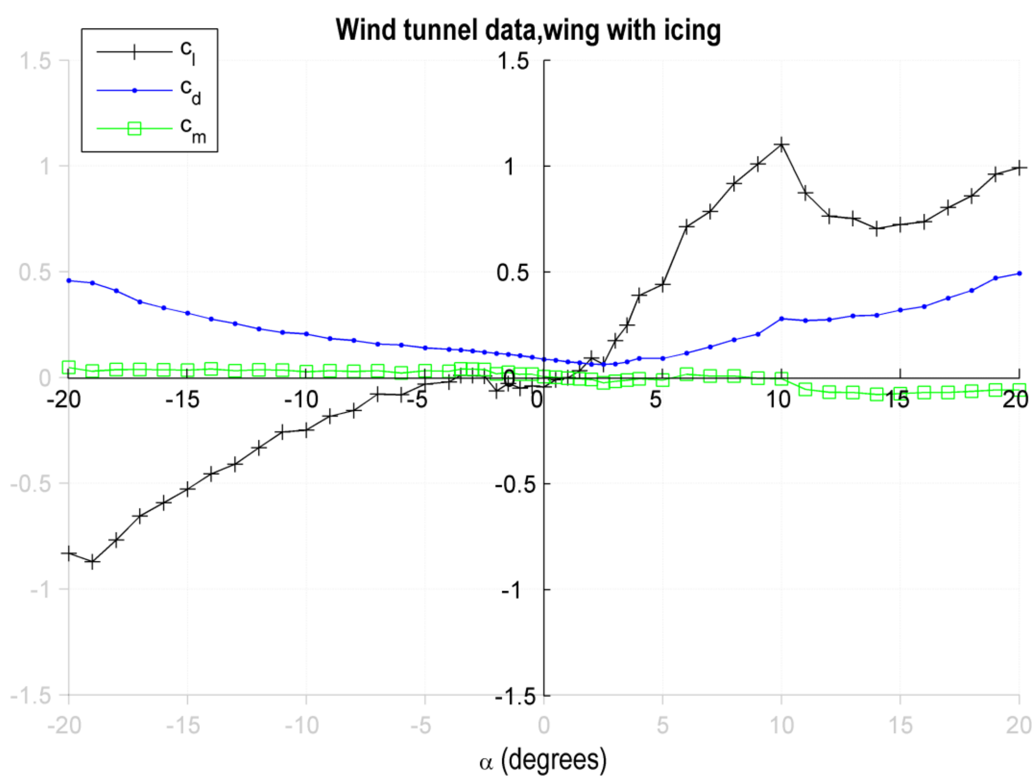

Figure 3.14 c_l, c_d, and c_m plotted versus α for a wing with icing. Re = $2.005 \cdot 10^5$, M_∞ = 0.0792

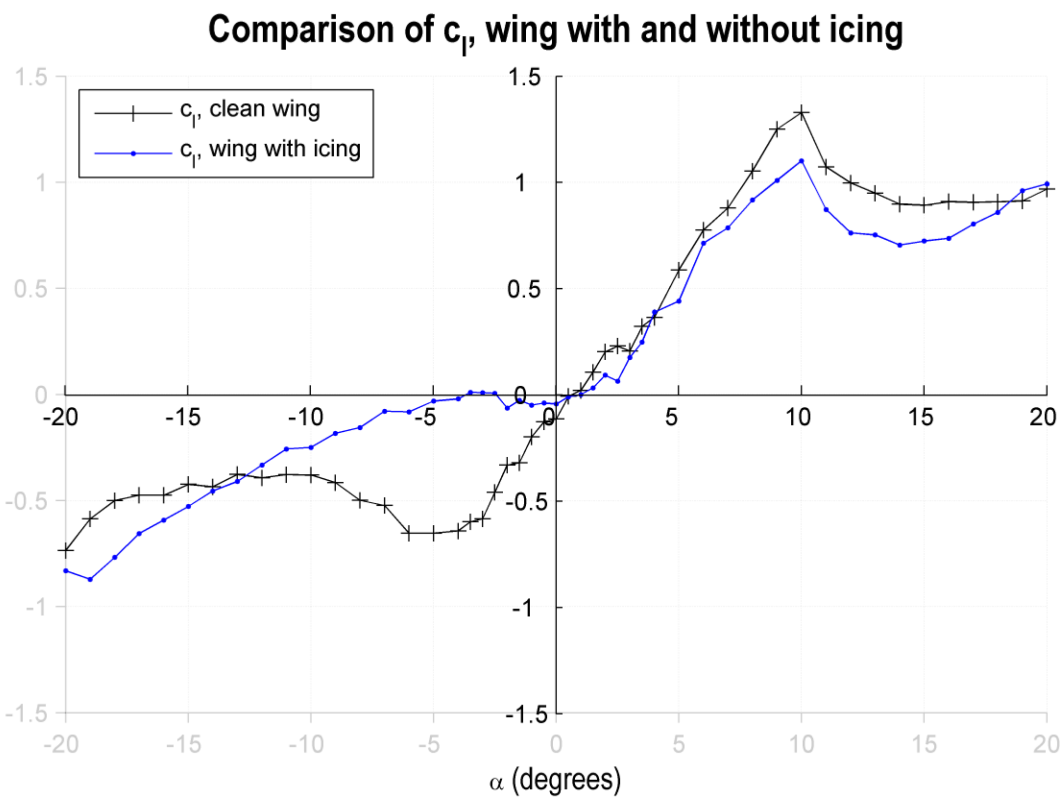

Figure 3.15 Comparison of c_l between a wing with and without icing. Re = $2.005 \cdot 10^5$, M_∞ = 0.0792

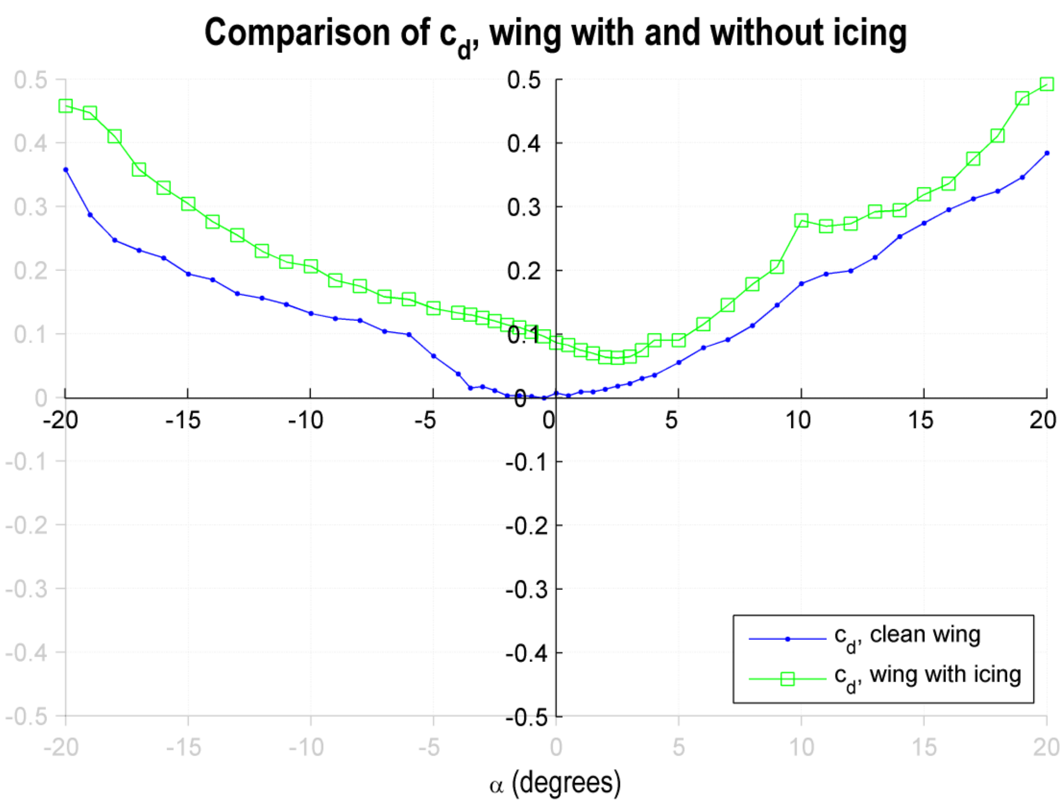

Figure 3.16 Comparison of c_d between a wing with and without icing. Re = $2.005 \cdot 10^5$, M_∞ = 0.0792

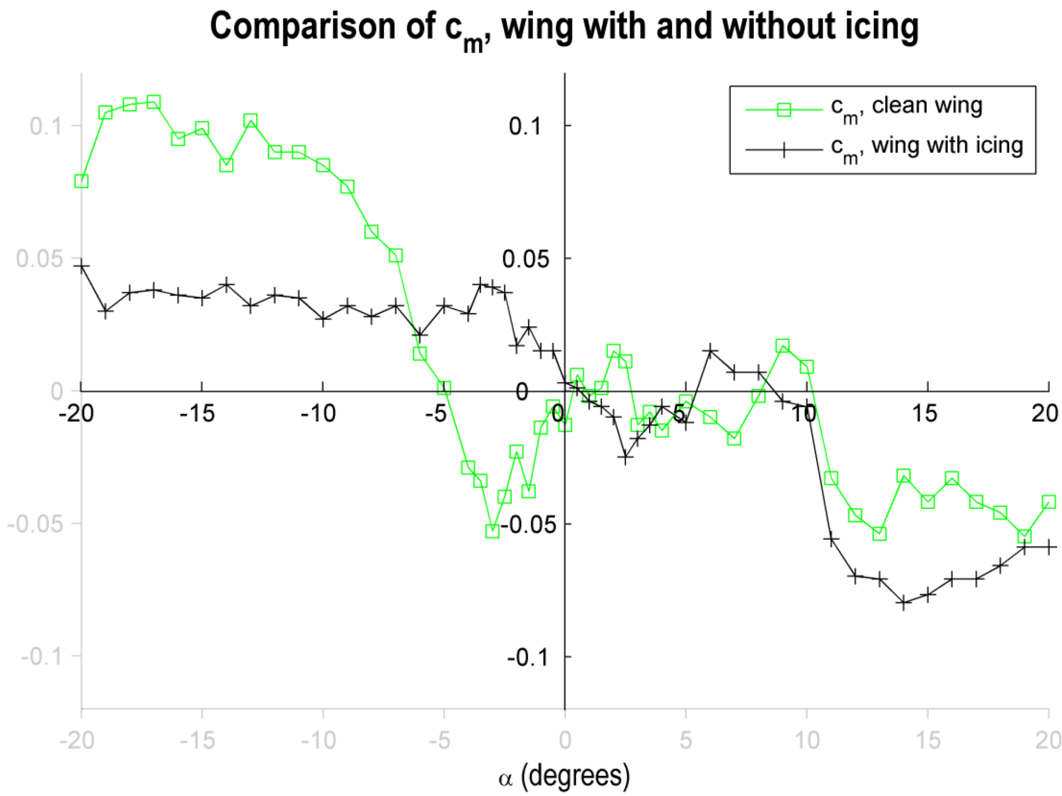

Figure 3.17 Comparison of c_m between a wing with and without icing, Re = 2.005 · 10^5, M_∞ = 0.0792

3.5 Discussion

3.5.1 Drag coefficient

The drag coefficient curve for both wings has approximately the same shape (Figure 3.16). The drag coefficient is high for high angles of attack and decreases when the angle of attack approaches zero, which is as expected. When the ice shape is mounted on the wing, the drag coefficient increases by a value that varies from 0.035 to 0.160. The smallest difference occurs at an angle of attack of 5 degrees (Figure 3.18). This is due to the shape of both coefficient curves when the drag coefficient approaches its minimum. Also, the difference in drag coefficients at positive angles of attack is smaller than at negative angles of attack. The reason for this becomes clear when looking at Figure 3.19.

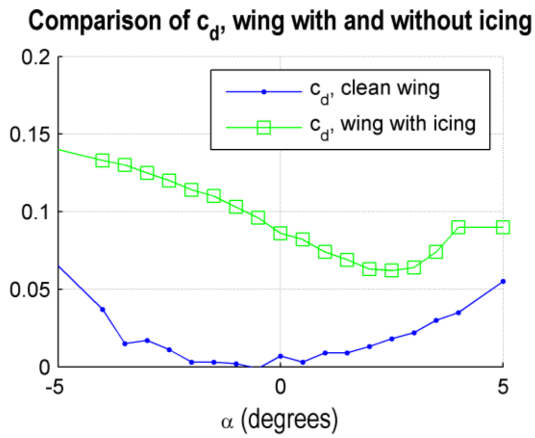

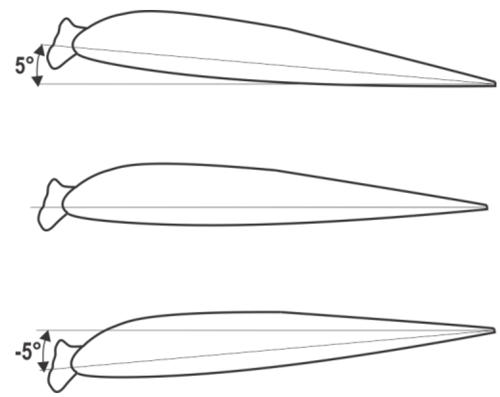

Figure 3.18 Comparison of c_d between a wing with and without icing. Re = 2.005 · 10^5, M_∞ = 0.0792

Figure 3.19 Wing with icing at an angle of attack of -5°, 0 and 5°

Because of the shape of the ice, the frontal area of the wing increases as the angle of attack becomes negative. This results in a higher value for the drag coefficient. When the angle of attack becomes positive, the ice shape becomes slightly smoother, so the difference in drag coefficient between the wing with and without icing becomes smaller here.

3.5.2 Lift coefficient

The lift coefficient for the clean wing (Figure 3.15) is mostly linear between -4 and 10 degrees (Figure 3.20). The maximum lift occurs at an angle of attack of 10 degrees. There are some points that slightly differ from the theoretical linear lift slope. The cause for this may be due to measurement errors. The lift slope for the wing with icing is can only be seen as linear between approximately 2 and 10 degrees. The value of the lift coefficient of the wing with icing in this region is slightly less than the value of the lift coefficient of the clean wing.

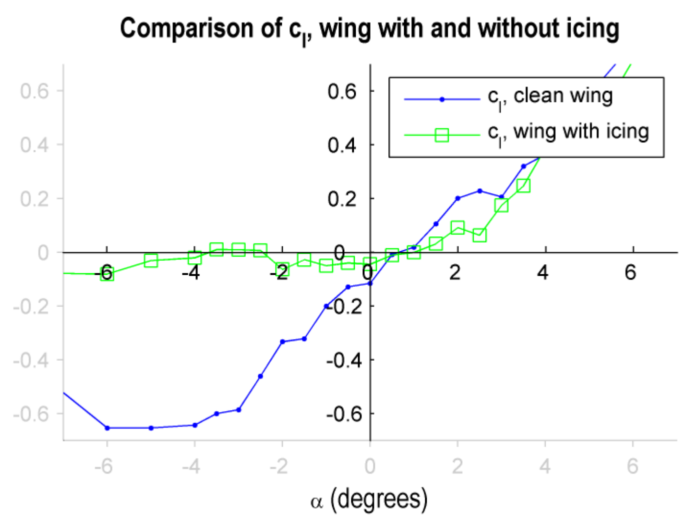

Figure 3.20 Comparison of c_l between a wing with and without icing. Re = 2.005 · 10^5, M_∞ = 0.0792

At angles of attack from -12 to 0 degrees, the value of c_l for the wing with icing becomes significantly lower than the value of c_l for the clean wing. The lift of the wing with icing approaches zero in this region. Again, this may be due to the shape of the ice (Figure 3.19).

The lift slope in the linear region of Figure 3.15 for both the clean wing and wing with icing can be calculated by using the following equation:

$$\frac{dc_l}{d\alpha} = \frac{c_{l,2} - c_{l,1}}{\alpha_2 - \alpha_1} \tag{3.15}$$

Where $c_{l,2}$ and $c_{l,1}$ are the lift coefficient at α_2 and α_1, respectively. α_2 is the maximum angle of the linear range of the (c_l, α) curve in radians and α_1 is the minimum angle of the linear range of the (c_l, α) curve in radians. Calculating the lift slope for the clean wing and wing with icing gives:

$$\frac{dc_l}{d\alpha}_{clean} = \frac{1.328 - (-0.643)}{0.1745 - (-0.0698)} = 2.56\,\pi \tag{3.16}$$

$$\frac{dc_l}{d\alpha}_{ice} = \frac{1.101 - 0.091}{0.1745 - 0.0349} = 2.30\,\pi \tag{3.17}$$

The linear range for the clean wing is taken from -4° to 10°, whereas the linear range for the wing with icing is taken from 2° to 10°. The lift slope for both the clean wing and wing with icing is higher than the theoretical 2π per radian. This deviation may be due to a measurement error in the calibration or the force meter itself.

Another value that deviates is $\alpha_{L=0}$. In theory, $\alpha_{L=0}$ for an ATR-72 wing should be negative, whereas $\alpha_{L=0}$ in Figure 3.15 is positive. This may be due to an error caused when the wing was mounted on the rotating plateau. If the wing is mounted at a slightly different angle, there will be a shift to the left or the right in the coefficient curves. If for instance the wing was already mounted at a slightly negative angle of attack, the lift coefficient curve shifts to the right which can cause $\alpha_{L=0}$ to be positive. Also, there is a slight tolerance in the rotating disc on which the angle of attack is determined which may contribute to the shift of the lift coefficient curve mentioned before.

3.5.3 Moment coefficient

The biggest difference in the moment coefficient is at large negative angles of attack. The value of the moment coefficient of the clean wing is twice as high as that of the wing with icing in this region. Also, at angles of attack from -5 degrees to 0 degrees c_m is negative for the clean wing but positive for the wing with icing. At positive angles of attack, both coefficient curves have approximately the same shape.

3.5.4 Error analysis

The force meter in the wind tunnel measures the axial and normal force and moment about the pitching axis in terms of a voltage drop. This is done for a certain period of time at every angle of attack. In this case, the voltage drop was measured every 0.1 second, over a time period of approximately 60 seconds. To obtain the axial and normal force and moment about the pitching axis, the average of these voltage drops is taken, which is then translated into the corresponding forces and moment using the correlation matrix, as described in chapter 3.3.4.

The maximum error in A, N and M can be determined by taking the minimum and maximum value of each measurement and plotting these values as errorbars. This results in Figure 3.21 to 3.23. The same can be done for the aerodynamic coefficients, which results in Figure 3.24 to 3.26.

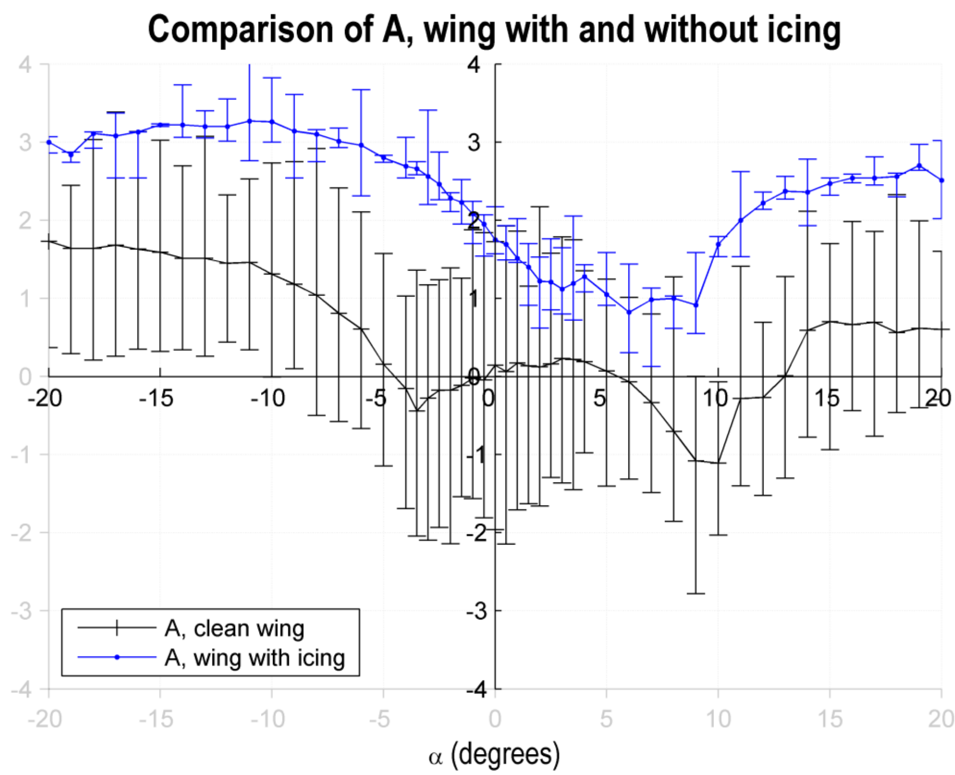

Figure 3.21 Comparison of the axial force A between a wing with and without icing, with minimum and maximum error.
Re = 2.005 · 10^5, M_∞ = 0.0792

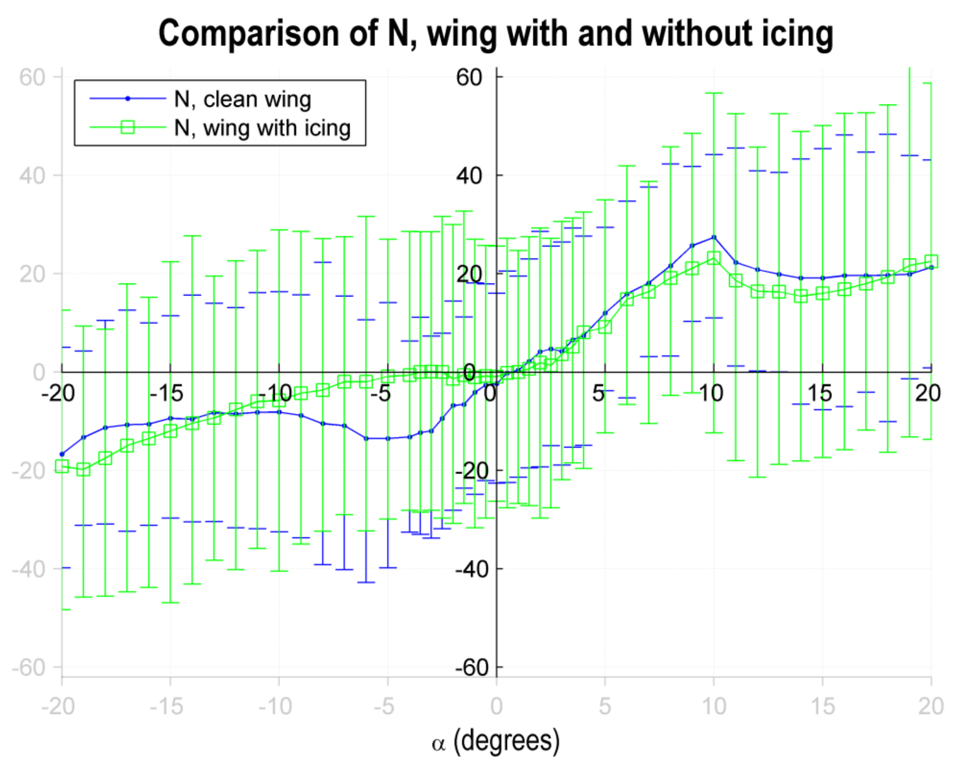

Figure 3.22 Comparison of the Normal force N between a wing with and without icing, with minimum and maximum error.
Re = 2.005 · 10^5, M_∞ = 0.0792

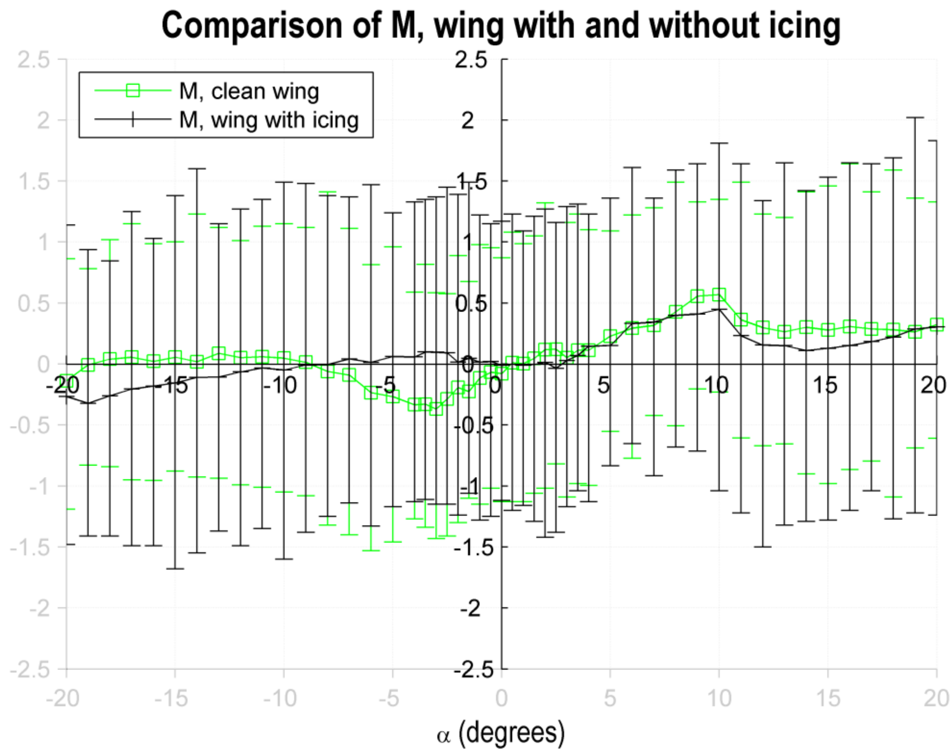

Figure 3.23 Comparison of the axial force A between a wing with and without icing, with minimum and maximum error.
Re = 2.005 · 10^5, M_∞ = 0.0792

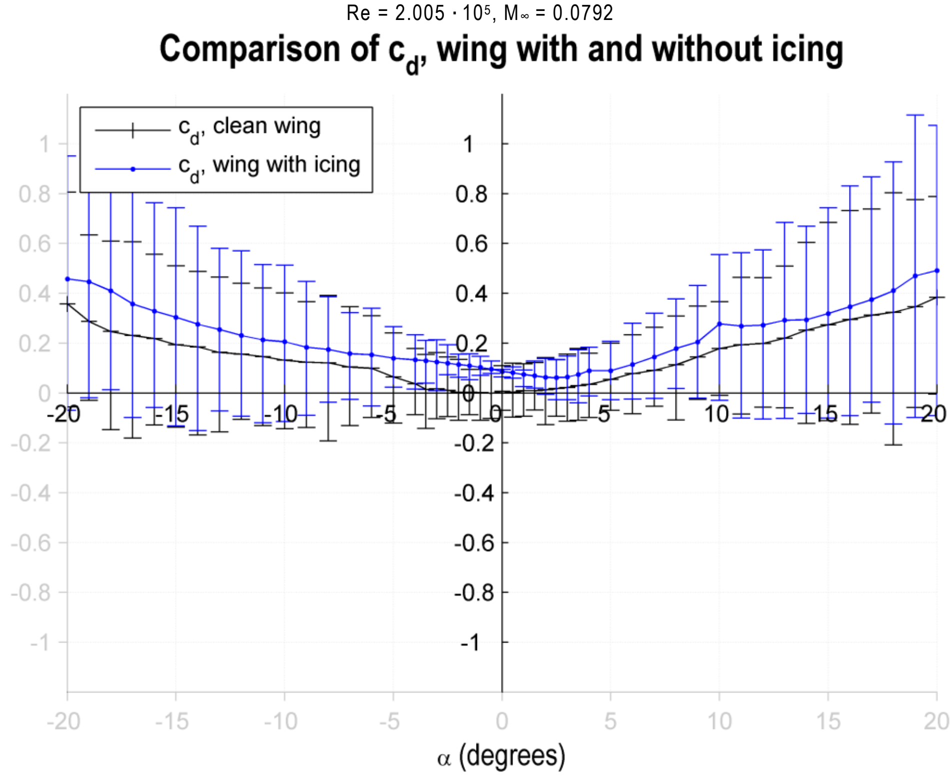

Figure 3.24 Comparison of the drag coefficient c_d between a wing with and without icing, with minimum and maximum error.
Re = 2.005 · 10^5, M_∞ = 0.0792

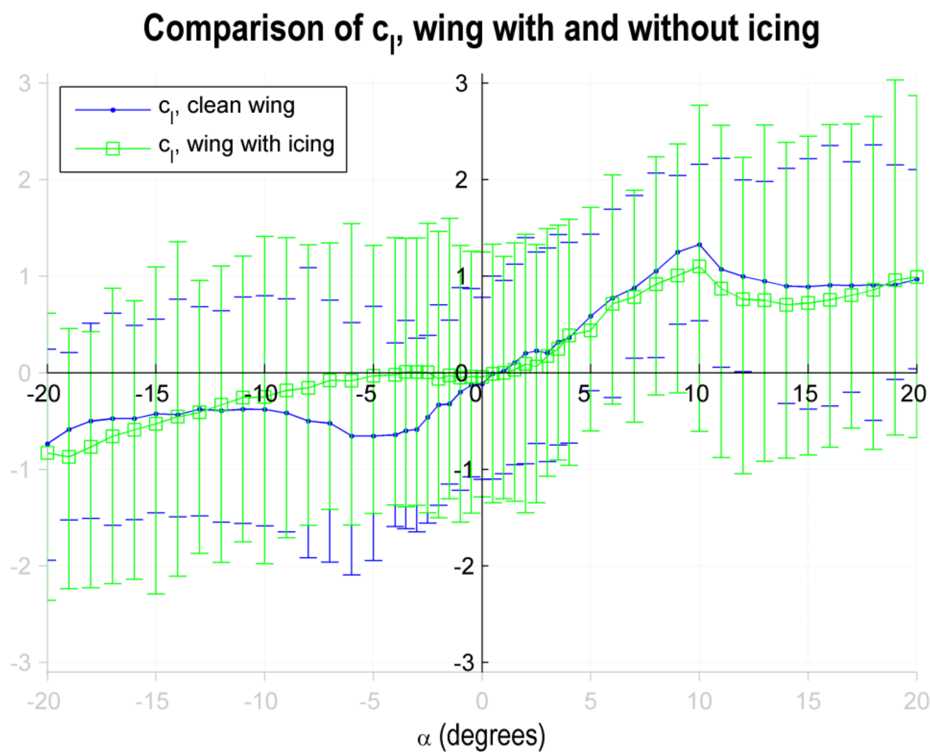

Figure 3.25 Comparison of the lift coefficient c_l between a clean wing and wing with icing, with minimum and maximum error. $Re = 2.005 \cdot 10^5$, $M_\infty = 0.0792$

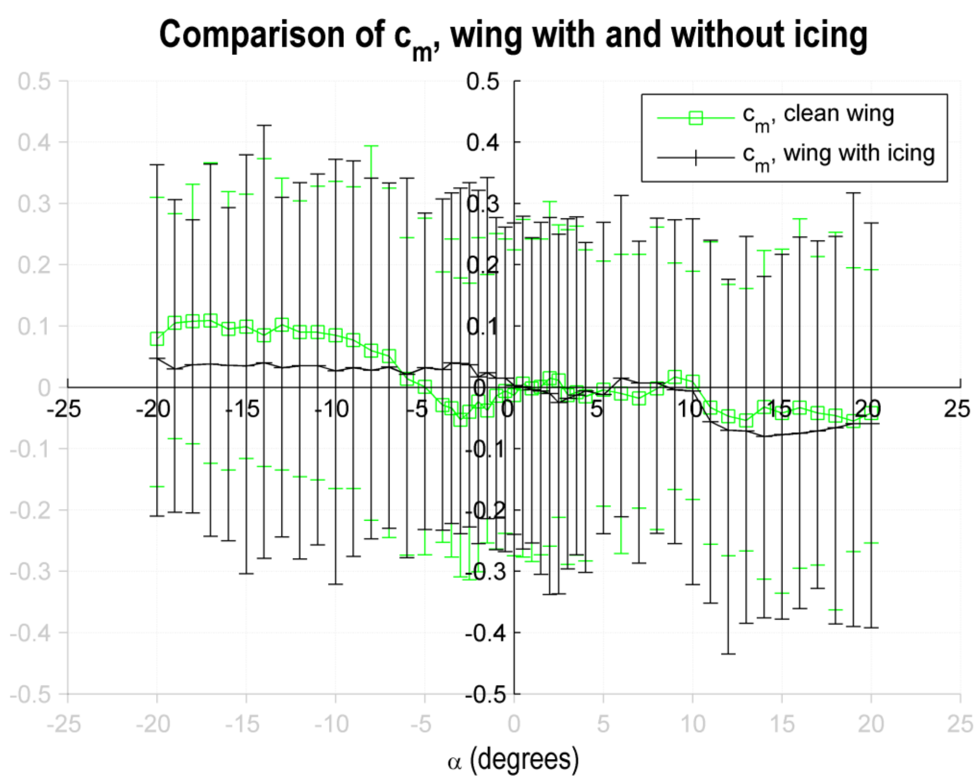

Figure 3.26 Comparison of the moment coefficient c_m between a clean wing and wing with icing, with minimum and maximum error. $Re = 2.005 \cdot 10^5$, $M_\infty = 0.0792$

Looking at Figure 3.24, 3.25 and 3.26, the maximum error on each coefficient is quite high. This arises from a periodical disturbance that occurred during the measurement. Because the amplitude of the periodic signal is quite high, the errorbars plotted in Figure 3.16, 3.17 and 3.18 are not really representative for the value the coefficients can have. Each measurement was done at a time interval of 60 seconds. Increasing this time will not have an effect on the length of the errorbars. However, it will cause a more precise average of the periodic signal. The error because of this effect will become lower as the time of measurement is increased.

4 Modeling

To obtain theoretical data on different quantities like the aerodynamic coefficients, streamlines or obtained ice shape, the ATR-72 airfoil will be analyzed using the program 2DFOIL(-ICE).

4.1 2DFOIL

4.1.1 Introduction

2DFOIL is a computer program that calculates the stationary flow solution around a closed contour. This closed contour is a two-dimensional airfoil, which is represented as a spline. A distribution of straight panels is created on this spline, with a source and dipole on every panel. The velocity at each point around the airfoil can be determined by solving the source- and dipole distribution. The pressure distribution can be determined using the Bernoulli-relation for stationary potential flow. The lift-, drag- and moment-coefficient can then be calculated using this pressure distribution. (Hospers, 2008) The free-stream conditions and geometry of the airfoil can be adjusted in an input file, located in the input folder of 2DFOIL. The windows command window is used to run 2DFOIL. When the simulation is completed, the results will be stored in multiple output files. An example input file can be found in Appendix A.

4.1.2 Results

To compare the results from the wind tunnel experiments with the modeled results, the clean ATR-72 airfoil will be modeled at the same environmental conditions as in the wind tunnel experiment. The resulting coefficient curves are given in Figure 4.1 to 4.3.

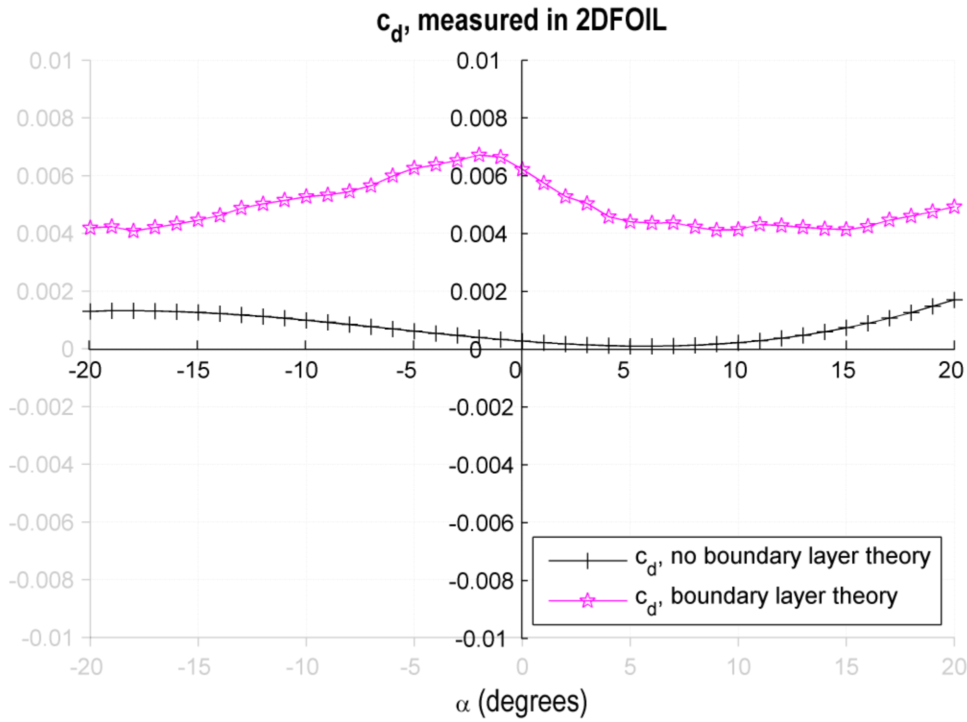

Figure 4.1 c_d, measured in 2DFOIL. Re = $2.005 \cdot 10^5$, $M_\infty = 0.0792$

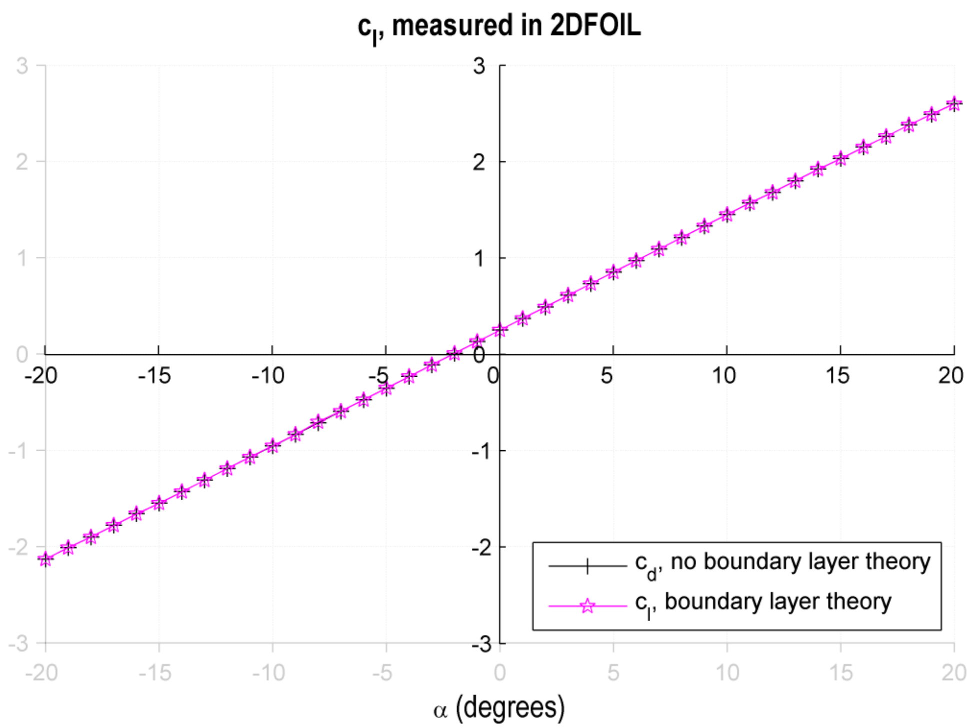

Figure 4.2 c_l, measured in 2DFOIL. Re = $2.005 \cdot 10^5$, $M_\infty = 0.0792$

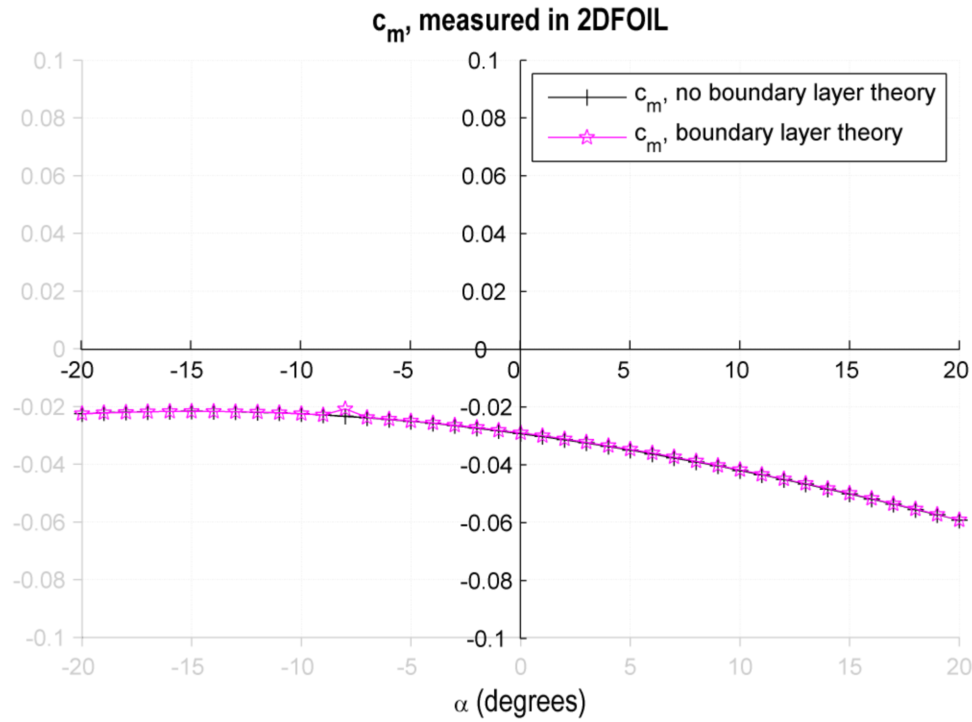

Figure 4.3 c_m, measured in 2DFOIL. Re = $2.005 \cdot 10^5$, $M_\infty = 0.0792$

4.1.3 Discussion

Looking at Figure 4.2 and 4.3, there is no visible difference between the results measured with boundary layer theory and the results measured without boundary layer theory for the lift- and moment coefficient. Only c_d had a higher value when it is measured using boundary layer theory (Figure 4.1). This difference is due to the fact that the skin friction will increase as the boundary layer theory is included. The lift slope of the lift coefficient curve can be calculated using Equation (3.15).

$$\frac{dc_l}{d\alpha} = \frac{c_{l,2}-c_{l,1}}{\alpha_2-\alpha_1} = \frac{2.60-(-2.13)}{0.3491-(-0.3491)} = 2.15\,\pi \qquad (4.1)$$

4.2 2DFOIL-ICE

4.2.1 Introduction

2DFOIL-ICE gives the possibility to compute ice accretions on airfoils. The ice accretion is calculated by specifying a wet flow. The droplet trajectories of this wet flow are calculated using a Lagrangian method. By employing this method the place and velocity of the droplets will be known at every position on their trajectory through the flow. A thermodynamic balance has to be solved to compute the ice accretion. This is done by solving the heat and mass balance for each of the control volumes associated with each panel used in the panel distribution. To include icing in the modeling, the air has to be specified as wet in the ATR-72 input file and droplet parameters have to be set which specify the droplet cloud characteristics. The droplet characteristics can be changed in the droplet input file. An example of this input file can be found in Appendix B. (Hospers, 2008)

4.2.2 Results

There are different parameters that influence the shape of the ice accretion. The effect of each parameter can be determined by varying one of the parameters, whilst keeping the other parameters constant. The results are given in chapter 4.2.2.1 to 4.2.2.8.

4.2.2.1 VARIABLE DROPLET DIAMETER

The first variable that has been varied is the droplet diameter. This parameter has been varied from 10 μm to 30 μm. The values of the other constants can be found in Table 4.1.

V_∞ (m/s)	T_{flow} (K)	Ambient air pressure (Pa)	α (°)	LWC (kg m^{-3})	Duration (s)	Droplet Diameter (m)
50	253.15	101325	0	3.0 ·10-3	1800	Variable

Table 4.1 Constants used to model the ice accretion on an ATR-72 airfoil, with variable droplet diameter

The resulting ice shapes can be found in Figure 4.4 and Figure 4.5, where Figure 4.5 is a close-up around the nose region.

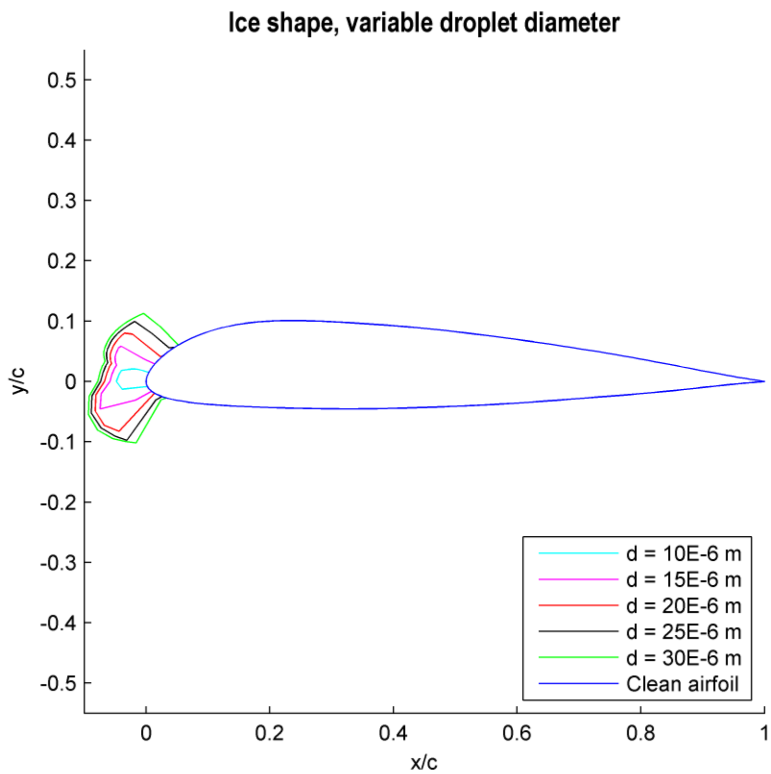

Figure 4.4 Results ice accretion, variable droplet diameter

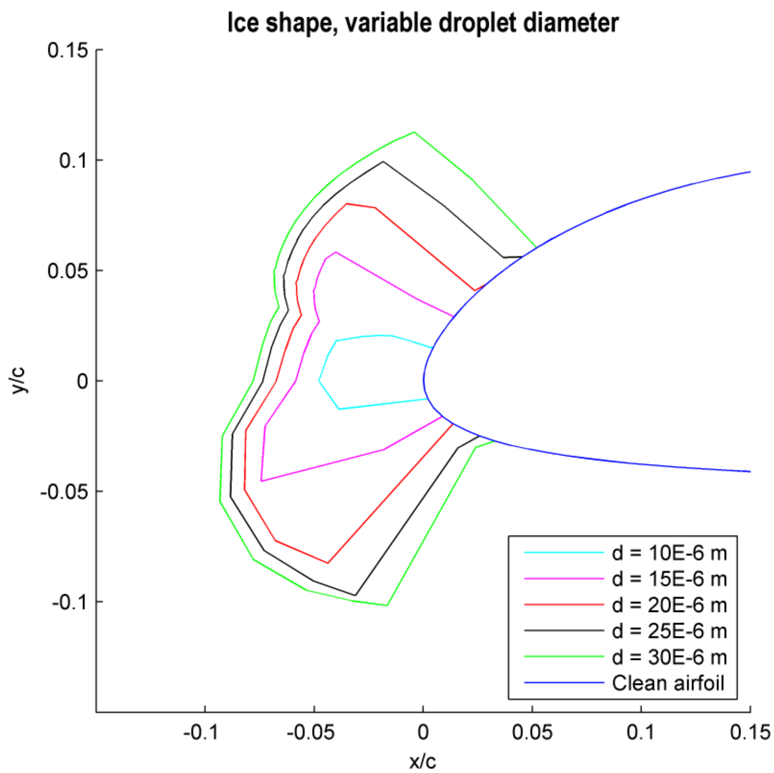

Figure 4.5 Results ice accretion, variable droplet diameter

Changing the droplet diameter results in different ice shapes. The larger the droplets, the larger the ice shape. The ice shape will also form on a larger area of the airfoil as the droplet size increases.

4.2.2.2 VARIABLE AMBIENT AIR TEMPERATURE

The next variable that has been varied is the ambient air temperature. This parameter has been varied from -25 °C to -5 °C. The values of the other constants can be found in Table 4.2.

V_∞ (m/s)	T_{flow} (K)	Ambient air pressure (Pa)	α (°)	LWC (kg m^{-3})	Duration (s)	Droplet Diameter (m)
50	Variable	101325	0	$3.0 \cdot 10^{-3}$	1800	$18 \cdot 10^{-6}$

Table 4.2 Constants used to model the ice accretion on an ATR-72 airfoil, with variable ambient air temperature

The resulting ice shapes can be found in Figure 4.6.

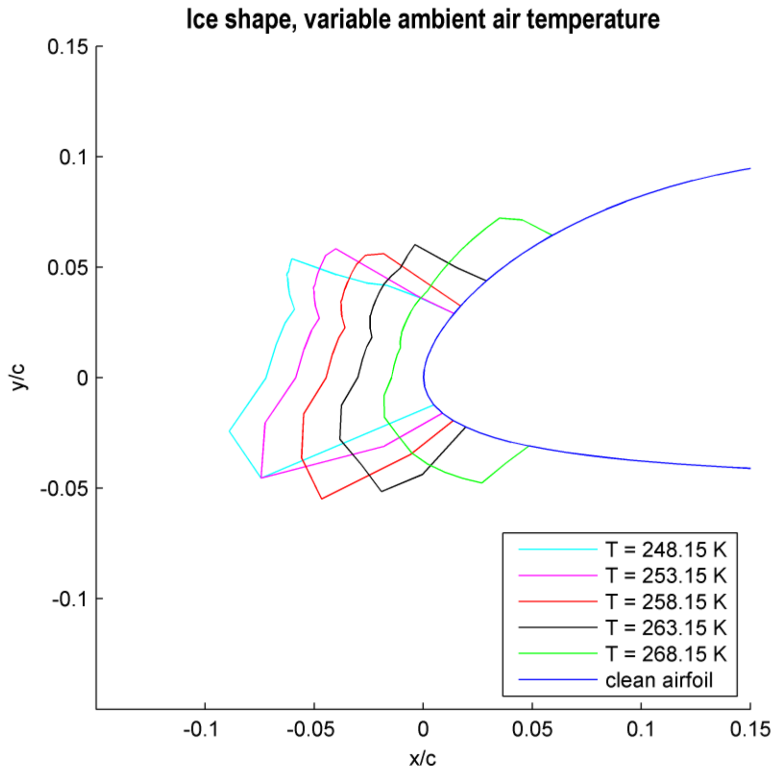

Figure 4.6 Results ice accretion, variable ambient air temperature

Increasing the ambient air temperature results in an ice shape that covers a larger area of the airfoil. This is due to the fact that an ambient air temperature that is closer to the freezing point of water will cause the droplets to freeze more slowly. Because the droplets freeze more slowly, they will have the chance to run further down the airfoil. Increasing the temperature also results in an airfoil that is more smooth.

4.2.2.3 VARIABLE DURATION OF SINGLE ICE ACCRETION STEP

The next variable that has been varied is the duration of a single ice accretion step, which has been varied from 60 to 7200 seconds. The values of the other constants can be found in Table 4.3.

V_∞ (m/s)	T_{flow} (K)	Ambient air pressure (Pa)	α (°)	LWC (kg m^{-3})	Duration (s)	Droplet Diameter (m)
50	253.15	101325	0	$3.0 \cdot 10^{-3}$	Variable	$18 \cdot 10^{-6}$

Table 4.3 Constants used to model the ice accretion on an ATR-72 airfoil, with variable duration of a single ice-accretion step

The resulting ice shapes can be found in Figure 4.7.

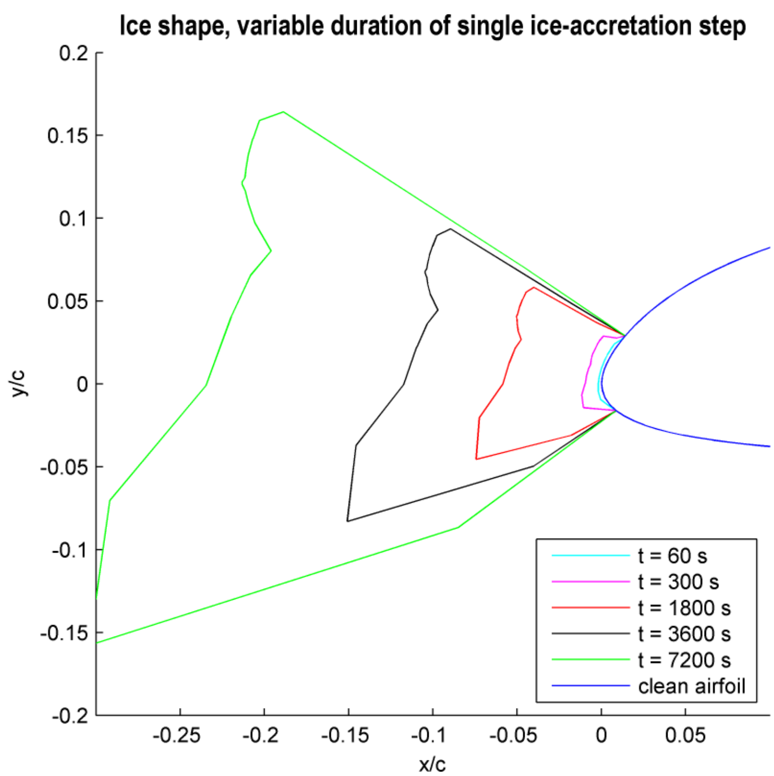

Figure 4.7 Results ice accretion, variable duration of a single ice-accretion step

Figure 4.7 shows that changing the time only has an effect on the size of the ice shape. Increasing the time results in a larger ice shape. However, the very large ice shapes modeled in Figure 4.7 will probably have broken off of the wing before they would have been able to reach this size.

4.2.2.4 VARIABLE LIQUID WATER CONTENT

The next variable that has been varied is the liquid water content, which was set from 1 g/m^3 to 3 g/m^3. The liquid water content is the amount of liquid water that is present in an icing cloud. The values of the other constants can be found in Table 4.4.

V_∞ (m/s)	T_{flow} (K)	Ambient air pressure (Pa)	α (°)	LWC (kg m^{-3})	Duration (s)	Droplet Diameter (m)
50	253.15	101325	0	Variable	1800	$18 \cdot 10^{-6}$

Table 4.4 Constants used to model the ice accretion on an ATR-72 airfoil, with variable liquid water content

The resulting ice shapes can be found in Figure 4.8.

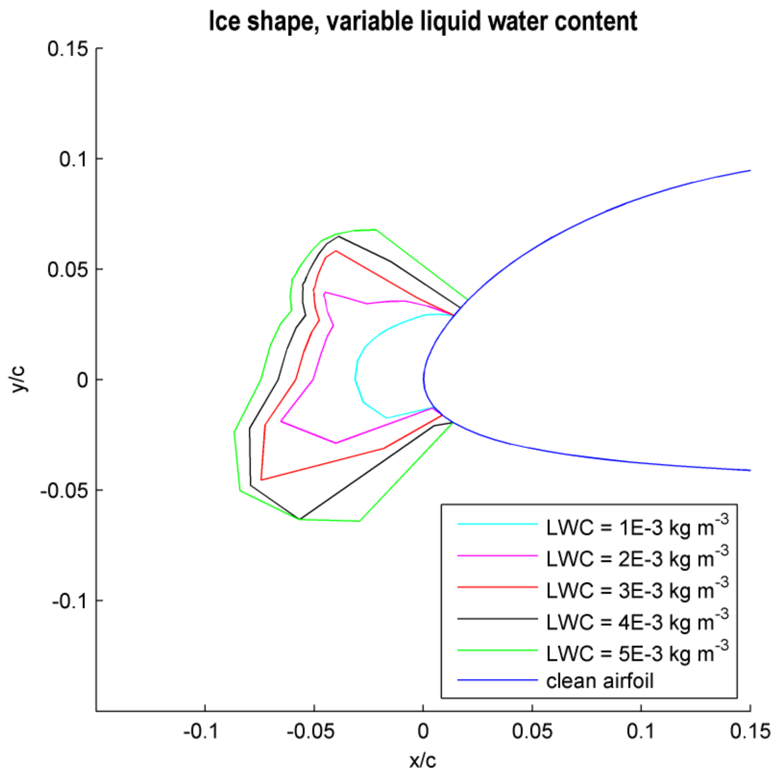

Figure 4.8 Results ice accretion, variable liquid water content

Figure 4.5 shows that the liquid water content has an effect on the shape and size of the ice. A higher value for the liquid water content results in a larger ice shape.

4.2.2.5 VARIABLE FREE-STREAM VELOCITY

The next variable that has been varied is the free-stream velocity, which was set from 20 m/s to 100 m/s. The values of the other constants can be found in Table 4.5.

V_∞ (m/s)	T_{flow} (K)	Ambient air pressure (Pa)	α (°)	LWC (kg m^{-3})	Duration (s)	Droplet Diameter (m)
Variable	253.15	101325	0	$3.0 \cdot 10^{-3}$	1800	$18 \cdot 10^{-6}$

Table 4.5 Constants used to model the ice accretion on an ATR-72 airfoil, with variable liquid water content

The resulting ice shapes can be found in Figure 4.9.

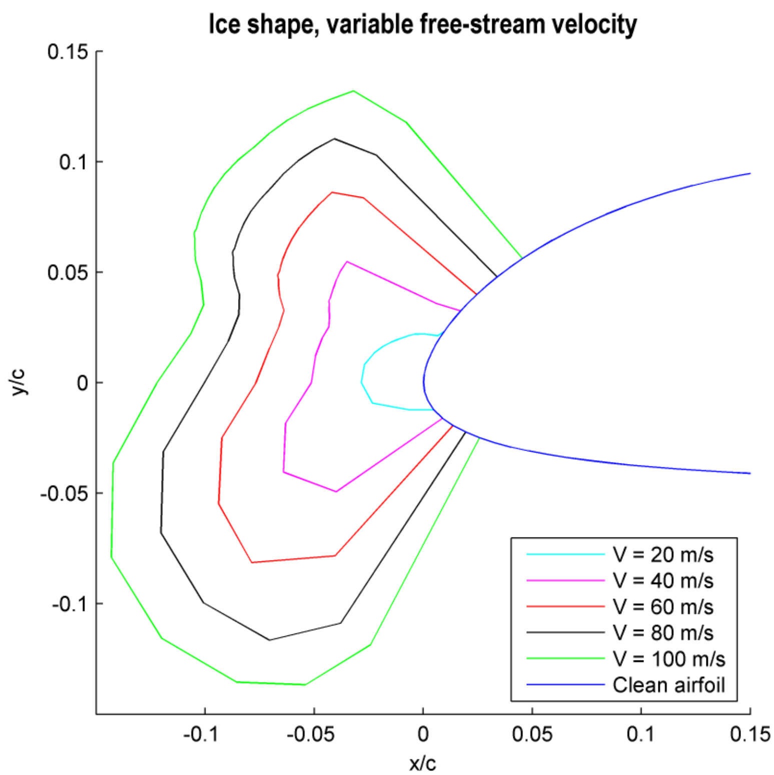

Figure 4.9 Results ice accretion, variable free-stream velocity

Figure 4.9 shows that the free-stream has an effect on the size of the ice. A higher value for the free-stream velocity results in a larger ice shape. The shape of each ice shape remains approximately the same.

4.2.2.6 VARIABLE ANGLE OF ATTACK

The next variable that has been varied is the angle of attack, which was set from -1 to 1°. The values of the other constants can be found in Table 4.6.

V_∞ (m/s)	T_{flow} (K)	Ambient air pressure (Pa)	α (°)	LWC (kg m^{-3})	Duration (s)	Droplet Diameter (m)
50	253.15	101325	Variable	$3.0 \cdot 10^{-3}$	1800	$18 \cdot 10^{-6}$

Table 4.6 Constants used to model the ice accretion on an ATR-72 airfoil, with variable liquid water content

The resulting ice shapes can be found in Figure 4.10.

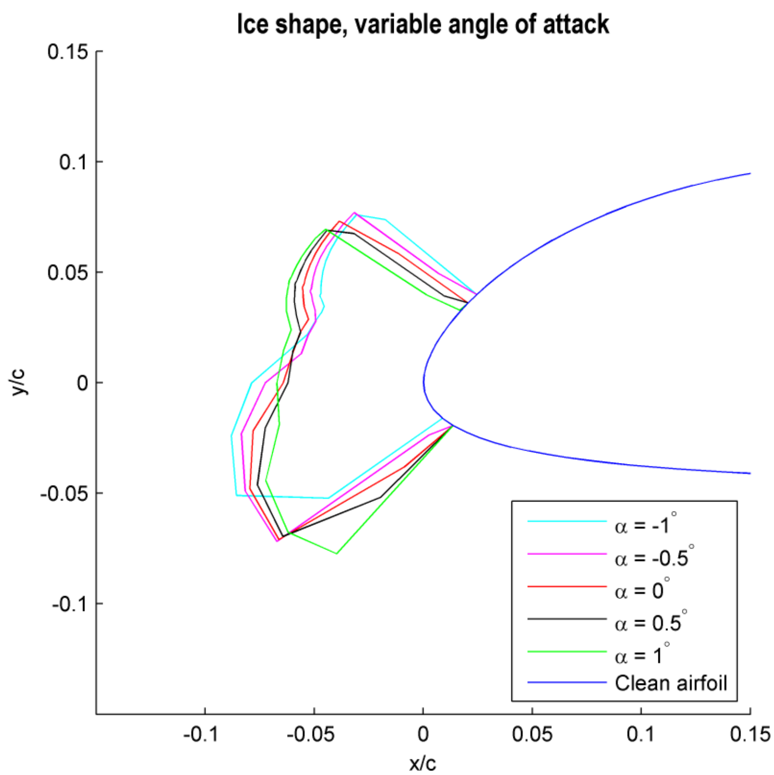

Figure 4.10 Results ice accretion, variable free-stream velocity

Figure 4.10 shows that the angle of attack has an effect on the shape of the ice. As the angle of attack increases, the position at which the ice is attached to the airfoil will shift counter-clockwise. Also, higher angles of attack will result in an ice shape with a larger frontal area.

4.2.2.7 NORMAL DISTRIBUTION WITH VARIABLE VARIANCE

For the next simulation, a normal distribution is used for the droplet diameter. The normal distribution divides the droplet cloud up into a specified number of normally distributed droplet sizes. This makes it possible to model a cloud with droplets of different diameters. However, using a normal distribution will greatly enhance the computation time. The variance of this normal distribution will be varied from 0.1 µm to 1 µm. The values of the other constants can be found in Table 4.7.

V_∞ (m/s)	T_{flow} (K)	Ambient air pressure (Pa)	α (°)	LWC (kg m^{-3})	Duration (s)	Droplet Diameter (m)
50	253.15	101325	0	$3.0 \cdot 10^{-3}$	1800	$18 \cdot 10^{-6}$

Table 4.7 Constants used to model the ice accretion on an ATR-72 airfoil, with variable liquid water content

The resulting ice shapes can be found in Figure 4.11.

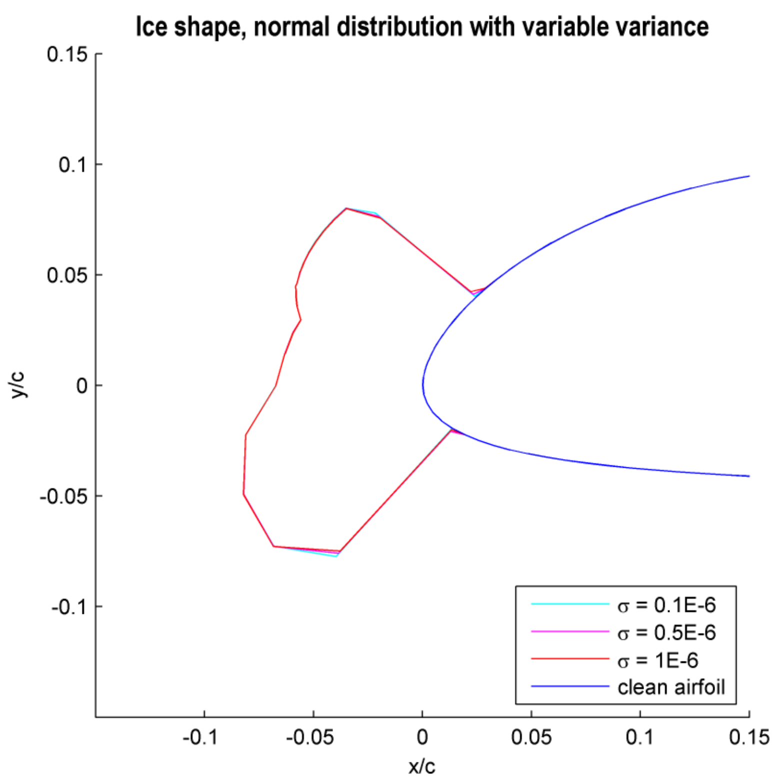

Figure 4.11 Resulting ice accretion, normal distribution with variable variance

The normal distribution with variable variance does not have a significant effect on the shape of the ice. This may change when the variance is higher than the variance used in these simulations. However, when these simulations were performed with 2DFOIL-ICE, the program could not compute the ice shape. This may be due to the fact that the program will encounter negative droplet diameters as the variance increases. It is expected that varying the normal distribution will have a larger effect when the droplets are significantly larger (>100µm, SLD).

4.2.2.8 COMPARISON WITH ORIGINAL ICE SHAPE

Now that the effects of each parameter are known, these parameters are varied to try to obtain the original ice shape used on the ATR-72 wing in the wind tunnel experiments. The value of each parameter is given in Table 4.8.

Ice shape	V_∞ (m/s)	T_{flow} (K)	Ambient air pressure (Pa)	α (°)	LWC (kg m^{-3})	Duration (s)	Droplet Diameter (m)
1	50	253.15	101325	-0.5	$3.0 \cdot 10^{-3}$	1800	$19 \cdot 10^{-6}$
2	50	253.15	101325	-0.5	$3.0 \cdot 10^{-3}$	1500	$19 \cdot 10^{-6}$
3	50	253.15	101325	-0.5	$2.5 \cdot 10^{-3}$	1500	$19 \cdot 10^{-6}$
4	50	256.15	101325	-0.5	$2.5 \cdot 10^{-3}$	1500	$19 \cdot 10^{-6}$
5	50	256.15	101325	-0.5	$2.5 \cdot 10^{-3}$	1500	$18 \cdot 10^{-6}$
6	50	258.15	101325	-0.5	$2.5 \cdot 10^{-3}$	1500	$18 \cdot 10^{-6}$
7	55	258.15	101325	-0.5	$2.5 \cdot 10^{-3}$	1500	$18 \cdot 10^{-6}$
8	55	258.15	101325	-0.5	$2.5 \cdot 10^{-3}$	1600	$17 \cdot 10^{-6}$

Table 4.8 Parameters used to model the ice accretion on an ATR-72 airfoil resulting in 8 different ice shapes

The resulting ice shapes are displayed in Figure 4.12 to 4.16.

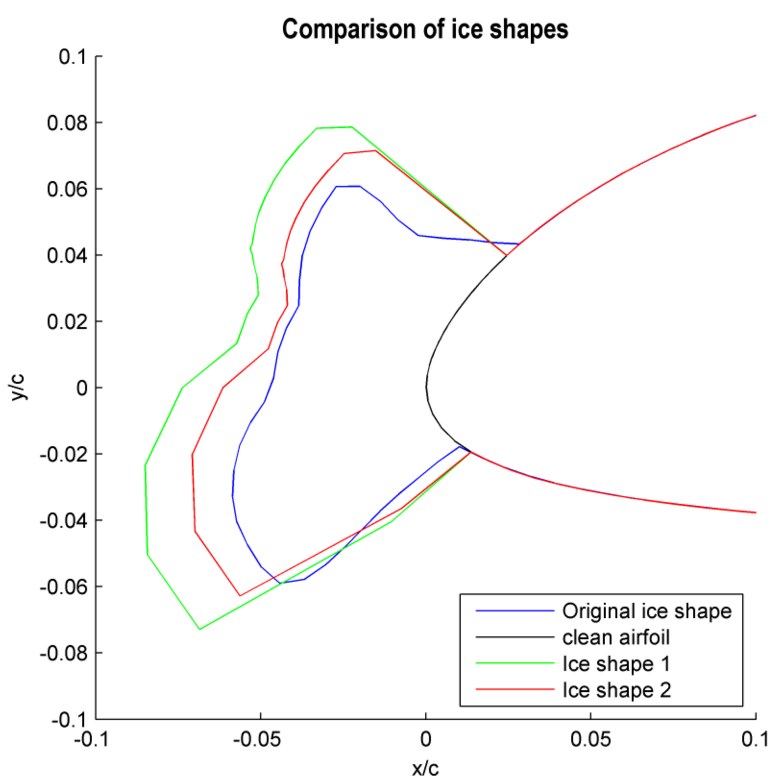

Figure 4.12 Comparison of original ice accretion on an ATR-72 wing with ice accretion computed with 2DFOIL-ICE

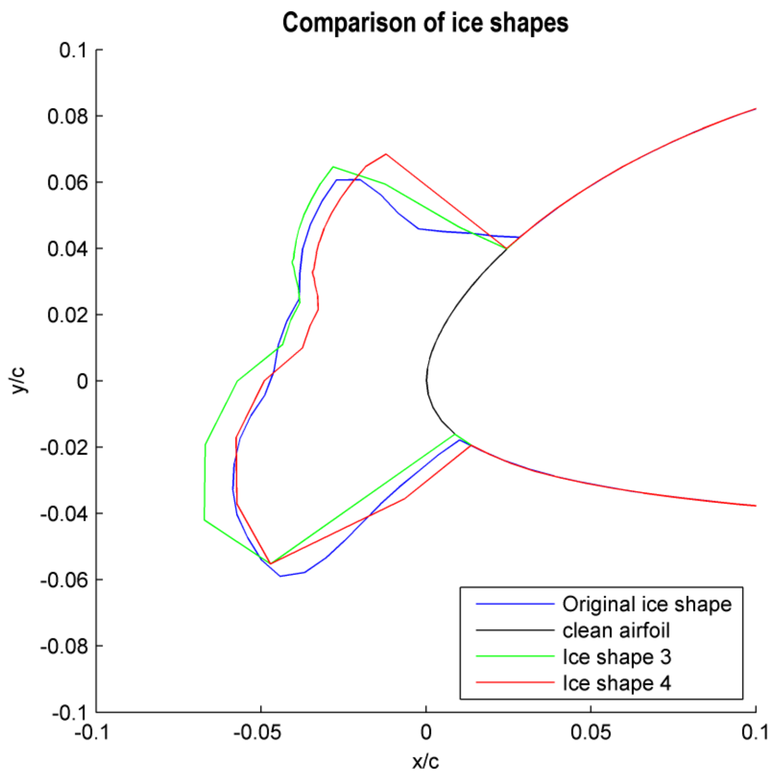

Figure 4.13 Comparison of original ice accretion on an ATR-72 wing with ice accretion computed with 2DFOIL-ICE

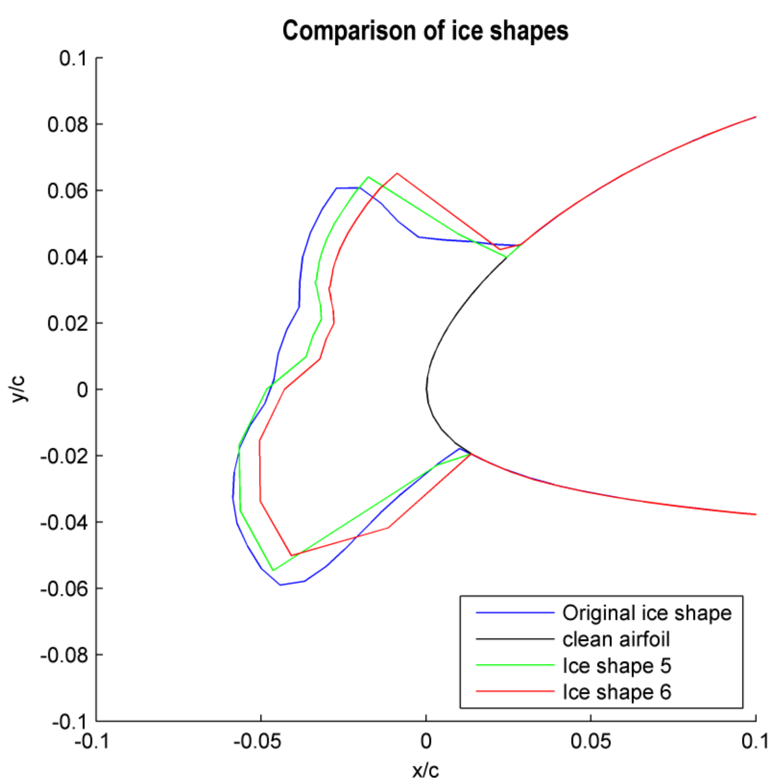

Figure 4.14 Comparison of original ice accretion on an ATR-72 wing with ice accretion computed with 2DFOIL-ICE

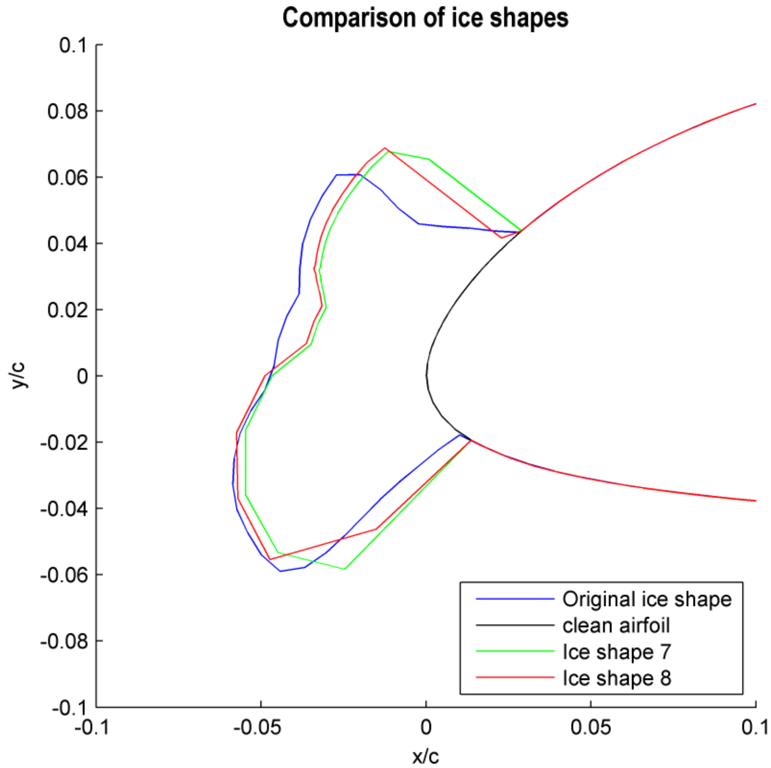

Figure 4.15 Comparison of original ice accretion on an ATR-72 wing with ice accretion computed with 2DFOIL-ICE

The ice shapes computed with 2DFOIL-ICE that have the most resemblance with the original ice shape used in the wind tunnel experiments, are ice shape 3 (Figure 3.13) and 5 (Figure 3.14).

4.2.3 Discussion

The conditions at which ice shapes 3 (Figure 3.11) and 5 (Figure 3.12) were formed are given in Table 4.10.

Ice shape	**V_∞** (m/s)	**T_{flow}** (K)	**Ambient air pressure** (Pa)	**α (°)**	**LWC (kg m^{-3})**	**Duration (s)**	**Droplet Diameter (m)**
3	50	253.15	101325	-0.5	$2.5 \cdot 10^{-3}$	1500	$19 \cdot 10^{-6}$
5	50	256.15	101325	-0.5	$2.5 \cdot 10^{-3}$	1500	$18 \cdot 10^{-6}$

Table 4.10 Parameters used to model ice shape 3 and 5

A temperature of 253.15 K corresponds to a geometric altitude of approximately 5400 meters, whereas a temperature of 256.15 K corresponds to a geometric altitude of approximately 4900 meters. The pressure at 5400 and 4900 meters are 51226 N/m^2 and 54773 N/m^2, respectively. (Anderson, 2007). An angle of attack of -0.5° could mean the plane is descent. The descent speed of an ATR-72-500 aircraft is approximately 110 m/s (Atlantic Sun Airways CAT A Pilot Procedures). This means a free-stream velocity of 50 m/s is probably too low. Droplets impinging on aircrafts are usually below 40-50 μm in diameter (Norde, 2013), so a droplet diameter of $18 \cdot 10^{-6}$ or $19 \cdot 10^{-6}$ m could be possible. Glaze ice generally forms at temperatures between 268 K and 273 K and at high airspeeds. This means the formation of ice shape 3 and 5 in the conditions in Table 4.10 are probably not possible in real life. Because there are many variables that can be changed, the ice shape used in the wind tunnel experiments could have been formed at completely different parameters. So the fact that the parameters in Table 4.10 are not realistic does not mean that the ice shape was created at unrealistic conditions.

5 Modeled versus Measured results

5.1 Introduction

The coefficient curves obtained with the numerical method can be plotted with the measured coefficient curves to compare the modeled with the measured data. This modeled data was obtained with 2DFOIL, with and without boundary layer theory. This results in Figure 5.1, 5.2 and 5.3.

5.2 Results

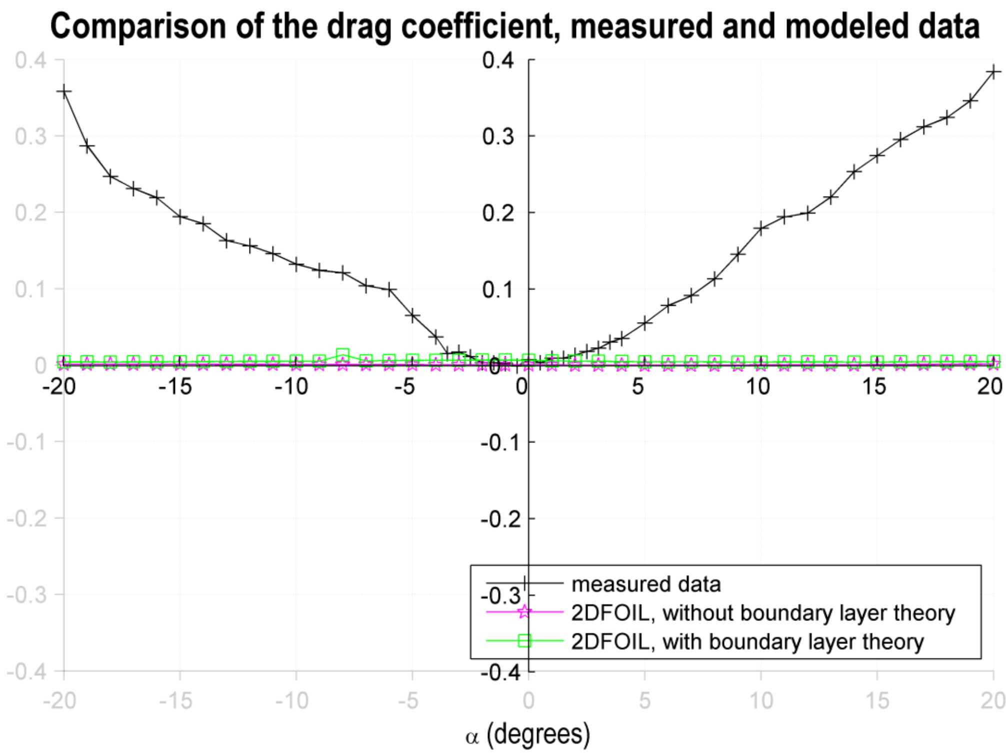

Figure 5.1 Comparison of the drag coefficient between the modeled and measured data.
Re = 2.005 · 10^5, M_∞ = 0.0792

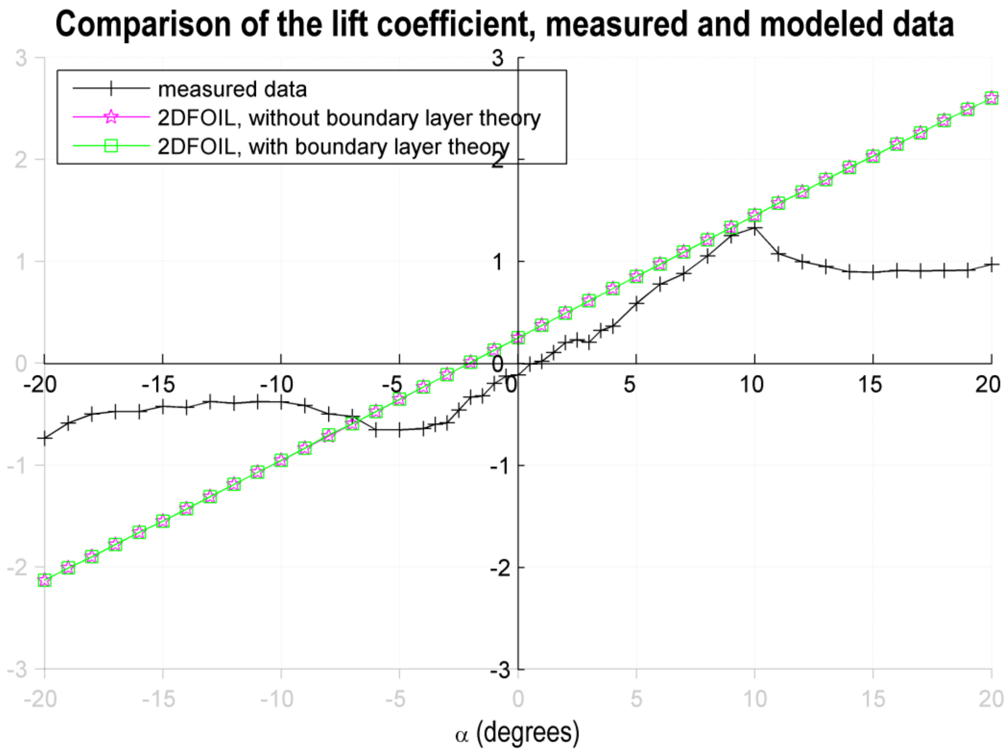

Figure 5.2 Comparison of the lift coefficient between the modeled and measured data.
Re = $2.005 \cdot 10^5$, $M_\infty = 0.0792$

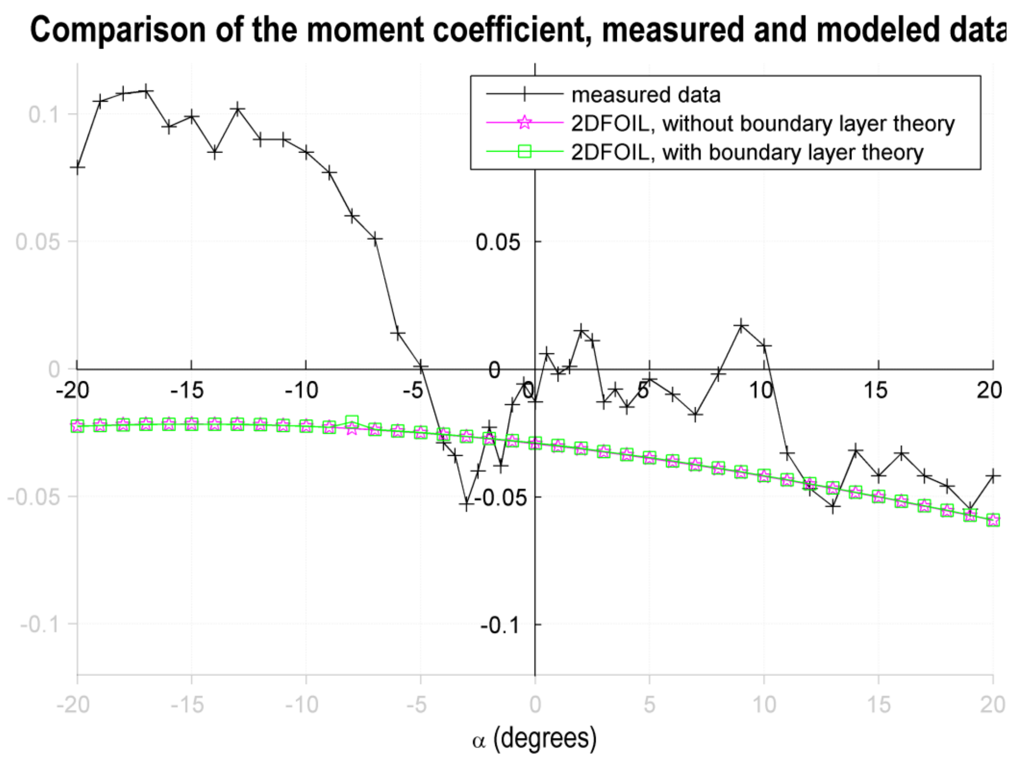

Figure 5.3 Comparison of the moment coefficient between the modeled and measured data.
Re = $2.005 \cdot 10^5$, $M_\infty = 0.0792$

5.3 Discussion

5.3.1 Drag coefficient

The modeled data for the drag coefficient is much lower than the measured data. The reason for this can be the fact that 2DFOIL does not take into account that the flow is viscous. This means only the form drag is calculated. On aerodynamic shapes, the share of form drag due to flow separation on the total drag is much lower than the share of viscous drag on the total drag (Anderson, 2007). When viscosity is taken into account, the drag will be significantly higher and more representative.

5.3.2 Lift coefficient

The lift coefficient calculated in 2DFOIL is slightly higher than the lift coefficient measured in the wind tunnel in the linear range of the coefficient curve. This may be due to the fact that the wing used in the wind tunnel is three-dimensional instead of two-dimensional. There are slight gaps at the end of the wing, which allows the effect of downwash. However, because this gap is very small, the effect of downwash is negligible. Also, the flow in the wind tunnel may not be as ideally laminar as the flow in 2DFOIL, which will cause a lower value for the lift. An effect 2DFOIL does not take into account is the viscosity. Because of this, there will be no flow separation in 2DFOIL. This flow separation will cause a reduced lift. Because there is no flow separation, there is also no maximum and minimum lift and the value for the lift coefficient is linear at all angles of attack in the modeled results.

Conclusion

The effect of the ice shape on the performance of the wing measured in the wind tunnel was significant. The wing experienced a slight decrease in lift at positive angles of attack. At negative angles of attack, the decrease in lift was significant. Also, the wing with ice experienced a decrease of $c_{l,max}$ of about 0.2. The drag coefficient of the wing with icing also experienced an increase at every angle of attack.

The validity of the wind tunnel experiments could be questioned, because the value of $dc_l/d\alpha$ was higher than the theoretical 2π and $\alpha_{L=0}$ was positive where it should be negative. However, because both the clean wing and wing with ice profile were tested in the same conditions, without changing anything on the experimental set-up, a comparison between both wings will be probably valid. The minimum and maximum error during the measurements was quite large because of a periodic signal that occurred during the measurements. The possible error because of this effect was reduced by increasing the measurement time.

The modeled results from 2DFOIL deviated from the results from the wind tunnel experiments. The lift coefficient matched the wind tunnel results the best. The lift coefficient modeled in 2DFOIL was slightly higher, but had no maximum and minimum value. The drag coefficient and moment coefficient came in no way close to the results from the wind tunnel experiment. This difference resulted from the fact that viscous effects are neglected in 2DFOIL.

2DFOIL was also not able to compute the flow field over the airfoil with icing, as it encountered multiple stagnation points.

Recommendations

2DFOIL was not able to compute the flow field over an airfoil with icing. By using a different ice shape that is more smooth, for instance a rime ice profile, this problem may be fixed. Another solution could be to use a different numerical method than 2DFOIL-ICE. This could be a program that uses Eulerian instead of Lagrangian droplet tracking. Different ice shapes can also be tested on the ATR-72 wing, to have a better view of the effects of icing on the performance of the wing.

The ice shape used in the wind tunnel experiments was formed at unknown parameters. By using an ice shape that was formed at know parameters, more can be said about the validity of the conditions at which the ice shape was formed.

Because the results from the wind tunnel were slightly questionable, the same wing with ice profile can be tested again in another wind tunnel. This may result in a smaller error in the data.

To get a better understanding for the reason of the change in drag and lift of a wing with ice accretion, a technique can be used to try and visualize what happens to the boundary layer as a result of the ice profile.

Acknowledgements

First of all I would like to thank Ellen Norde for all the help and advice in the past weeks. The feedback during the weekly discussions and the proofreading of my report really helped me finish my report.

I also thank Harry Hoeijmakers for his help in finding a subject for my bachelor assignment and for his advice and feedback on my report.

I would also like to thank Wouter den Breeijen and Herman Stobbe for their help during the wind tunnel experiments.

Finally I would like to thank the department Engineering Fluid Dynamics for letting me use the wind tunnel.

Bibliography

Anderson, J. D. (2007). *Fundamentals of Aerodynamics* (4th ed.). New York: McGraw Hill .

ATR aircraft products, ATR 72-500 series. (n.d.). Retrieved April 2014, 2014, from www.atraircraft.com: http://www.atraircraft.com/products/atr-72-500.html

Aviation Safety Network. (n.d.). Retrieved June 24, 2014, from Roselawn accident 31 October 1994: http://aviation-safety.net/database/record.php?id=19941031-1&lang=nl

Feiertag, T. (n.d.). *Atlantic Sun Airways CAT A Pilot Procedures*. Retrieved June 30, 2014, from Atlantic Sun Airways: http://www.atlanticsunairways.com/training/checklist_atr72.pdf

Fluids orifices, Nozzles, Venturies. (n.d.). Retrieved April 04, 2014, from www.roymech.co.uk: http://www.roymech.co.uk/Related/Fluids/Fluids_Or_No_Ven.html

Hospers, J. (2008). *Manual for 2DFOIL-ICE.* Enschede: University of Twente.

Hospers, J., & Hoeijmakers, H. (2010). Eulerian Method for Ice Accretion on Multiple-Element Airfoils. *7th International Conference on Multiphase Flow, ICMF 2010* (pp. 1-2). Tampa, Florida: Faculty of Engineering Technology, group of Engineering Fluid Dynamics, University of Twente, the Netherlands.

Loading Data into MATLAB for Plotting. (n.d.). Retrieved May 06, 2014, from http://web.cecs.pdx.edu/: http://web.cecs.pdx.edu/~gerry/MATLAB/plotting/loadingPlotData.html#loadAndPlot

NASA Icing Branch. (2014, 3 June). Retrieved April 14, 2014, from http://icebox.grc.nasa.gov/: http://icebox.grc.nasa.gov/gallery/images/C95_03918.html

Norde, E. (2013). *Splashing Model for Impact of Supercooled Large Droplets on a Thin Liquid Film.* Enschede: Faculty of Engineering Technology, Group Engineering Fluid Dynamics.

Norris, G. (2013, September 2). *Core Engine Icing Strikes Russian 747-8F*. Retrieved April 04, 2014, from www.aviationweek.com: http://www.aviationweek.com/Article.aspx?id=/article-xml/AW_09_02_2013_p20-610669.xml

Appendix A

```
INPUT-FILE for multi-element airfoil, ATR-72
----------------------------------------------------------------------
nseg   nsegw   restart   iter
   2       1    .f.        1
cfl0   refl   yref
 2.0    1.0    0.0
----------------------------------------------------------------------
ANGLE OF ATTACK (degrees) FREE-STREAM VELOCITY (m/s) WET/DRY AIR (1/0)
-4                   25.38                       0
----------------------------------------------------------------------
REFERENCE LENGTH (= CHORD LENGTH (in output designated by "c"))
1.0
----------------------------------------------------------------------
NOSE RADIUS AIRFOIL (R/CHORD LENGTH)
PUT 0.0 TO LET 2DFOIL-ICE CALCULATE THE NOSE RADIUS
0.0
----------------------------------------------------------------------
ANGLE BOUNDING RANGE OF APPROXIMATION FRoSSLING (degrees)
TOP:
45.0
BOTTOM:
45.0
----------------------------------------------------------------------
COORDINATES MOMENT REFERENCE CENTER (X,Y relative to chord)
0.250   0.0
----------------------------------------------------------------------
AMBIENT AIR TEMPERATURE (K)
294.35
AMBIENT AIR PRESSURE (Pa)
100489.0
LIQUID WATER CONTENT, LWC (kg/m^3)
2.5e-3
RELATIVE HUMIDITY (0.0 is 0.0 percent, 1.0 is 100 percent)
1.d0
DROPLET DIAMETER (m) (> 10 micron)
19e-6   ### This needs to be set in droplets.inp
----------------------------------------------------------------------
NUMBER OF ICE-ACCRETION STEPS/LAYERS (1,2,...)
1
DURATION OF SINGLE ICE-ACCRETION STEP (seconds)
1200
----------------------------------------------------------------------
FACTOR TO ACCOUNT FOR ROUGHNESS ICE SURFACE
2.0
----------------------------------------------------------------------
REPANELLING PARAMETERS:
TURNING ANGLE (MAX ANGLE BETWEEN CONSECUTIVE PANELS)
6.0
DSMIN (MINIMUM PANEL SIZE, [m]/REFL/TOTAL ARCLENGTH) - NOT IN USE
0.0003
----------------------------------------------------------------------
TO ACTIVATE THE ANTI-ICING SYSTEM SET SWITCH-A TO 1
IF SWITCHED ON,
  EITHER
    SET THE TEMPERATURE CONSTANT BETWEEN
    THE BOUNDARIES OF THE PROTECTED SURFACE, SET SWITCH-T TO 1
    AND SET THE WALL TEMPERATURE TO A VALUE > 273.15 K
    AT THE SAME TIME: SET SWITCH-Q TO 0, AND HEAT FLUX TO '-'
  OR
    SET THE HEAT FLUX THROUGH THE AIRFOIL SKIN, GIVE PAD DISTRIBUTION
    SET SWITCH-Q TO 1 AND SET POWER DENSITY DISTRIBUTION
    AT THE SAME TIME: SET SWITCH-T TO 0, AND WALL TEMPERATURE TO '-'
```

```
ELSE
  ALL INPUT LINES FOR ANTI-ICING SYSTEM ARE IGNORED
----------------------------------------------------------------------
SWITCH-A 1/0
0
----------------------------------------------------------------------
  SWITCH-T 1/0
  0
    WALL TEMPERATURE >273.15/-
    278.15
    -
    SET THE BOUNDARIES FOR THE PROTECTED SURFACE:
    A POSITIVE ARC LENGTH COORDINATE FOR TOP EDGE IS
    NORMALIZED WITH THE ARC LENGTH FROM NOSE TO
    TRAILING EDGE ALONG THE UPPER SIDE,
    A NEGATIVE VALUE WITH THE ARC LENGTH OF THE LOWER SIDE.
    TOP EDGE:
    0.18
    -
    A POSITIVE ARC LENGTH COORDINATE FOR BOTTOM EDGE IS
    NORMALIZED WITH THE ARC LENGTH FROM NOSE TO
    TRAILING EDGE ALONG THE LOWER SIDE,
    A NEGATIVE VALUE WITH THE ARC LENGTH OF THE UPPER SIDE.
    BOTTOM EDGE:
    0.18
----------------------------------------------------------------------
  SWITCH-Q 1/0
  1
    NUMBER OF PADS
    7
    WRAP POSITION PADS s-s_nose (cm) AND POWER DENSITY (kW/m^2)
    -9.3599 -5.5499 9.920
    -5.5499 -3.0099 10.230
    -3.0099 -0.4699 32.550
    -0.4699  1.4351 46.500
     1.4351  3.9751 18.600
     3.9751  6.5151 6.975
     6.5151 10.3251 10.230
----------------------------------------------------------------------
  SWITCH-EV 1/0
  0
----------------------------------------------------------------------
STREAMLINES OVER AIRFOIL:
NUMBER OF STREAMLINES
3
AXIS SYSTEM IN THE NOSE, X ALONG THE CHORD, Y POSITIVE UPWARDS
XSTART/CHORD = -1.0, YSTART/CHORD TOP STREAMLINE =
0.05
XSTART/CHORD = -1.0, YSTART/CHORD BOTTOM STREAMLINE =
-0.15
----------------------------------------------------------------------
DROPLET TRAJECTORIES
NUMBER OF RELEASED DROPLETS TO FIND CATCH EFFICIENCY AIRFOIL
ONE DROPLET RELEASE POINT FOR EVERY # OF PANELS IN IMPINGEMENT REGION,
RECOMMENDED VALUE BETWEEN 1.0 AND 3.0:
2.0
RELEASE POINTS:
XSTART/CHORD = -1.5, YSTART/CHORD TOP DROPLET =
0.1
XSTART/CHORD = -1.5, YSTART/CHORD MIDDLE DROPLET =
0.0
XSTART/CHORD = -1.5, YSTART/CHORD BOTTOM DROPLET =
-0.1
TYPE OF DISTRIBUTION RELEASE POINTS (DOUBLE-COSINE 1/LINEAR 0)
1
----------------------------------------------------------------------
FOR DETERMINING Hc ALONG CONTOUR, SET FCTR
FCTR MULTIPLIED WITH LENGTH FIRST INTERVAL (LAMINAR EXPRESSION FOR Hc)
GIVES THE POINT FROM WHERE TURBULENT EXPRESSION FOR Hc APPLIES
TRANSITION OCCURS BETWEEN THESE TWO POINTS
FCTR
```

```
3.0
----------------------------------------------------------------------
nwkpr   nfield   nrespr1   nrespr2   nrespr3   nrespr4
   50        0         1         1         1      5000
----------------------------------------------------------------------
SEGMENT INFORMATION:
 ni nps iws iedg1 iedgn iabut1 iabutn iflow idist itype   q   xm   ra
141 200  1   0     0      2      2     0     4     0   0.0  1.0  0.5
  2   0  2   0     0      1      1     2     3     0   0.0  0.5  0.5
X(i)                Y(i)
1.000000000000000   0.000000000000000
0.992738602646094   -0.00048074427063
0.983540316642514   -0.00118915277588
0.969544365596244   -0.00237942200712
0.953880651570187   -0.00388777957064
0.936480297810779   -0.00570983079411
0.918038494147381   -0.00774241162711
0.898851211547601   -0.00989448841628
0.879264781426716   -0.01207403482001
0.859497785294865   -0.01421085602513
0.839663286835377   -0.01626009915813
0.819783224025315   -0.01820033298003
0.799827311257098   -0.02002988198654
0.779749860857985   -0.02176441646259
0.759525558109220   -0.02343103140662
0.739166829505933   -0.02505937497312
0.718715350177473   -0.02667387806009
0.698225403135116   -0.02828690351241
0.677755702987196   -0.02989294588683
0.657359258340578   -0.03147019149320
0.637065759284178   -0.03299114582677
0.616874084742227   -0.03443234997120
0.596757493283579   -0.03577706362085
0.576671716195291   -0.03701744848761
0.556572624537571   -0.03815737067130
0.536438576559559   -0.03920748045135
0.516271910348848   -0.04017541726367
0.496079555886971   -0.04106330311826
0.475862864588416   -0.04187344658855
0.455629849884481   -0.04261142685871
0.435408551099917   -0.04328093120314
0.415240716974733   -0.04387731820913
0.395162942071854   -0.04438690912361
0.375191321842854   -0.04479045493967
0.355314123946211   -0.04506801508912
0.335492651741833   -0.04520455765129
0.315672246424364   -0.04519497263481
0.295801876323276   -0.04504605229521
0.275853836676549   -0.04477360534508
0.255834662669958   -0.04439681293634
0.235788686650195   -0.04393341368834
0.215800704325584   -0.04339534893877
0.195996087546162   -0.04278419541786
0.176535554651343   -0.04209021148613
0.157610796688060   -0.04129737708798
0.139444038973819   -0.04038995871135
0.122280615038768   -0.03935596064964
0.106360521565505   -0.03818948413657
0.091871685034008   -0.03689479697563
0.078909936113603   -0.03548906455727
0.067468555210106   -0.03400006882367
0.057457089508764   -0.03245778750407
0.048738006797585   -0.03088074726136
0.041165169357621   -0.02926825740586
0.034603276723449   -0.02761012960360
0.028925419983014   -0.02590287477881
0.024007610868604   -0.02415402291964
0.019731685645567   -0.02237477847790
0.015993409371584   -0.02056935093611
0.012713120026129   -0.01872669400085
0.009845213824173   -0.01682221593685
```

0.007376018262836	-0.01483173790620
0.005306052735641	-0.01274818510054
0.003628545605074	-0.01058868320200
0.002319921155940	-0.00838632262617
0.001346244985083	-0.00617225709067
0.000676303083481	-0.00396182864333
0.000290227884584	-0.00175158298621
0.000178650314900	0.000477124214412
0.000334369202947	0.002752205968893
0.000746318566497	0.005102559700352
0.001403114831888	0.007549465021747
0.002300461075284	0.010103533341745
0.003443325383560	0.012769800325907
0.004844260803569	0.015556125814495
0.006523317423993	0.018478149553846
0.008509078046011	0.021557943175143
0.010838467900653	0.024817886412997
0.013555969619017	0.028274294355874
0.016712829907286	0.031935462496937
0.020367399507509	0.035805488928240
0.024589851052850	0.039890746982750
0.029468456932163	0.044201455242766
0.035103867349006	0.048740537262465
0.041584542055770	0.053483938156607
0.048961364829944	0.058370895948548
0.057246793496699	0.063315876908259
0.066436102543795	0.068230074516675
0.076519509707260	0.073031044877628
0.087468668035094	0.077636939657823
0.099222974126620	0.081962129686442
0.111702913241088	0.085925762304946
0.124836674546228	0.089464398163588
0.138573172831793	0.092536246569498
0.152881084600747	0.095118081813552
0.167746274100391	0.097201962629845
0.183168952634261	0.098793456338896
0.199157811597789	0.099909761262988
0.215723254423246	0.100577818693139
0.232870258510829	0.100833166477683
0.250589226326249	0.100718827879972
0.268848715511916	0.100282977957248
0.287595604161830	0.099575670352821
0.306759940093438	0.098645921452625
0.326257841674643	0.097539062976455
0.345993209459745	0.096293358780870
0.365863825413821	0.094936476219919
0.385771399640833	0.093483605531594
0.405631616436637	0.091936577082511
0.425386629025404	0.090282864867689
0.445020863725414	0.088498222040328
0.464569603432627	0.086555582259196
0.484110455241005	0.084436220325875
0.503736297991178	0.082138924884266
0.523516701016475	0.079683947208953
0.543466478945504	0.077108080590323
0.563538919035379	0.074451323239050
0.583648433760313	0.071740436022094
0.603713749240521	0.068978798506892
0.623696543643252	0.066149869384987
0.643612196457276	0.063230971396537
0.663508200052818	0.060208876496112
0.683423144074338	0.057087579897806
0.703357314082368	0.053881719507672
0.723278561509117	0.050603000822525
0.743149867038820	0.047252531598098
0.762951540801325	0.043821400692482
0.782689991175563	0.040295081018753
0.802396728555143	0.036659825564344
0.822113207051303	0.032912088764131
0.841856348063323	0.029068636054624
0.861582377034959	0.025171737869517

```
0.881177801920053   0.021287357506669
0.900472915581178   0.017497748763125
0.919272603333617   0.013887369104505
0.937323796279996   0.010536404698980
0.954414443968348   0.007494636286089
0.969868543285625   0.004856608926669
0.983712075569415   0.002583668766316
0.992814663609308   0.001123213796333
1.000000000000000   0.000000000000000
ytopdr   ymiddr   ybotdr
  0.10    -0.01    -0.10
X(i)                Y(i)
1.000000000000000   0.000000000000000
2.000000000000000   0.000000000000000
Vortex core position:
2.000000000000000   100000
```

Appendix B

```
INPUT-FILE for droplet distribution
----------------------------------------------------------------------
1      droplet input form, 1 = single, 2 = normal distr., 3 = manual
50     idropsize

----------------------------------------------------------------------
THIS SECTION IS ONLY USED FOR SINGLE DROPLET OR NORMAL DISTRIBUTION
----------------------------------------------------------------------
droplet diameter (m)   variance (sigma, NOT sigma**2)
17E-06                 1.5E-06

----------------------------------------------------------------------
THIS SECTION IS ONLY USED FOR MANUAL DROPLET INPUT
----------------------------------------------------------------------
droplet size           droplet fraction
----------------------------------------------------------------------
4.95000E-04    1.43997E-04
4.85000E-04    2.21842E-04
4.75000E-04    3.34616E-04
4.65000E-04    4.94327E-04
4.55000E-04    7.15485E-04
4.45000E-04    1.01498E-03
4.35000E-04    1.41166E-03
4.25000E-04    1.92560E-03
4.15000E-04    2.57699E-03
4.05000E-04    3.38464E-03
3.95000E-04    4.36418E-03
3.85000E-04    5.52614E-03
3.75000E-04    6.87391E-03
3.65000E-04    8.40191E-03
3.55000E-04    1.00942E-02
3.45000E-04    1.19235E-02
3.35000E-04    1.38515E-02
3.25000E-04    1.58292E-02
3.15000E-04    1.77990E-02
3.05000E-04    1.96973E-02
2.95000E-04    2.14577E-02
2.85000E-04    2.30146E-02
2.75000E-04    2.43076E-02
2.65000E-04    2.52847E-02
2.55000E-04    2.59058E-02
2.45000E-04    2.61451E-02
2.35000E-04    2.59926E-02
2.25000E-04    2.54545E-02
2.15000E-04    2.45529E-02
2.05000E-04    2.33236E-02
1.95000E-04    2.18145E-02
1.85000E-04    2.00819E-02
1.75000E-04    1.81876E-02
1.65000E-04    1.61954E-02
1.55000E-04    1.41679E-02
1.45000E-04    1.21637E-02
1.35000E-04    1.02350E-02
1.25000E-04    8.42611E-03
1.15000E-04    6.77504E-03
1.05000E-04    5.33162E-03
9.50000E-05    4.25859E-03
8.50000E-05    4.22753E-03
7.50000E-05    7.45058E-03
6.50000E-05    1.90082E-02
5.50000E-05    4.55422E-02
```

4.50000E-05	8.66136E-02
3.50000E-05	1.22562E-01
2.50000E-05	1.20305E-01
1.50000E-05	7.02018E-02
5.00000E-06	1.44279E-02

Appendix C

		Averages of logged samples			Loads			Aerodynamic coefficients		
α(°)	α(rad)	Chan1 (V/V)	Chan2 (V/V)	Chan3 (V/V)	A (N)	N (N)	M (Nm)	c_d	c_l	c_m
-20	-0.34906585	4.8509E-05	-2.3231E-04	-1.4069E-04	1.73E+00	-1.67E+01	-1.38E-01	0.358	-0.736	0.079
-19	-0.331612558	5.3740E-05	-2.1576E-04	-1.3006E-04	1.64E+00	-1.33E+01	-7.16E-03	0.287	-0.587	0.105
-18	-0.314159265	5.3842E-05	-1.9752E-04	-1.2557E-04	1.64E+00	-1.13E+01	3.97E-02	0.247	-0.500	0.108
-17	-0.296705973	5.4403E-05	-1.9201E-04	-1.2644E-04	1.68E+00	-1.07E+01	5.51E-02	0.231	-0.475	0.109
-16	-0.27925268	4.9750E-05	-1.8070E-04	-1.2258E-04	1.63E+00	-1.06E+01	2.23E-02	0.219	-0.475	0.095
-15	-0.261799388	4.9868E-05	-1.7115E-04	-1.1744E-04	1.59E+00	-9.40E+00	5.52E-02	0.194	-0.424	0.099
-14	-0.244346095	4.5207E-05	-1.6286E-04	-1.1278E-04	1.51E+00	-9.56E+00	1.89E-02	0.185	-0.435	0.085
-13	-0.226892803	4.9701E-05	-1.6205E-04	-1.1094E-04	1.51E+00	-8.27E+00	8.71E-02	0.163	-0.377	0.102
-12	-0.20943951	4.5605E-05	-1.5588E-04	-1.0717E-04	1.45E+00	-8.53E+00	5.23E-02	0.156	-0.393	0.090
-11	-0.191986218	4.5610E-05	-1.5212E-04	-1.0691E-04	1.46E+00	-8.16E+00	5.99E-02	0.146	-0.378	0.090
-10	-0.174532925	4.2489E-05	-1.4821E-04	-9.8034E-05	1.31E+00	-8.14E+00	4.81E-02	0.132	-0.380	0.085
-9	-0.157079633	3.8985E-05	-1.4914E-04	-9.1930E-05	1.18E+00	-8.80E+00	1.48E-02	0.124	-0.416	0.077
-8	-0.13962634	3.3072E-05	-1.5381E-04	-8.6593E-05	1.04E+00	-1.05E+01	-6.05E-02	0.121	-0.499	0.060
-7	-0.122173048	2.8200E-05	-1.5173E-04	-7.4283E-05	8.07E-01	-1.09E+01	-9.04E-02	0.104	-0.523	0.051
-6	-0.104719755	1.6015E-05	-1.5139E-04	-6.6256E-05	6.07E-01	-1.35E+01	-2.35E-01	0.099	-0.654	0.014
-5	-0.087266463	7.2318E-06	-1.4080E-04	-4.0355E-05	1.57E-01	-1.35E+01	-2.67E-01	0.065	-0.654	0.001
-4	-0.06981317	-4.9632E-06	-1.1616E-04	-1.9999E-05	-1.56E-01	-1.32E+01	-3.34E-01	0.037	-0.643	-0.029
-3.5	-0.061086524	-9.9894E-06	-1.0263E-04	-1.8707E-06	-4.41E-01	-1.23E+01	-3.30E-01	0.015	-0.600	-0.034
-3	-0.052359878	-1.3739E-05	-8.6225E-05	-8.3818E-06	-2.79E-01	-1.20E+01	-3.69E-01	0.017	-0.586	-0.053
-2.5	-0.043633231	-9.9408E-06	-6.8790E-05	-9.0130E-06	-1.77E-01	-9.43E+00	-2.86E-01	0.011	-0.461	-0.040
-2	-0.034906585	-6.0106E-06	-5.3873E-05	-4.3655E-06	-1.76E-01	-6.81E+00	-1.93E-01	0.003	-0.333	-0.023
-1.5	-0.026179939	-9.9604E-06	-4.0316E-05	-5.7633E-06	-1.16E-01	-6.59E+00	-2.26E-01	0.003	-0.322	-0.038
-1	-0.017453293	-2.6023E-06	-3.2785E-05	-7.2475E-06	-2.24E-02	-4.10E+00	-1.15E-01	0.002	-0.200	-0.014
-0.5	-0.008726646	-1.2020E-06	-2.3134E-05	-3.1766E-06	-4.62E-02	-2.64E+00	-6.73E-02	-0.001	-0.129	-0.006
0	0	-1.2219E-06	-1.5455E-05	-1.2266E-05	1.43E-01	-2.37E+00	-7.81E-02	0.007	-0.116	-0.013
0.5	0.008726646	2.5602E-06	-6.4932E-06	-4.3687E-06	6.20E-02	-1.85E-01	1.15E-02	0.003	-0.009	0.006
1	0.017453293	1.0297E-06	5.7315E-06	-8.1510E-06	1.70E-01	3.99E-01	2.62E-03	0.009	0.019	-0.002
1.5	0.026179939	9.4545E-07	2.1562E-05	-2.3793E-06	1.35E-01	2.15E+00	4.59E-02	0.009	0.105	0.001
2	0.034906585	4.0125E-06	3.2064E-05	1.7860E-06	1.21E-01	4.12E+00	1.18E-01	0.013	0.201	0.015
2.5	0.043633231	3.1876E-06	4.0332E-05	1.3883E-06	1.58E-01	4.67E+00	1.21E-01	0.018	0.228	0.011
3	0.052359878	-3.0930E-06	5.3602E-05	-1.3156E-06	2.28E-01	4.22E+00	5.19E-02	0.022	0.205	-0.013
3.5	0.061086524	-2.5834E-06	7.4275E-05	4.2327E-06	2.19E-01	6.57E+00	1.12E-01	0.030	0.320	-0.008
4	0.06981317	-5.3134E-06	8.8742E-05	8.5401E-06	1.90E-01	7.46E+00	1.12E-01	0.035	0.363	-0.015
5	0.087266463	-5.3502E-06	1.2875E-04	2.5090E-05	6.77E-02	1.20E+01	2.29E-01	0.055	0.586	-0.004
6	0.104719755	-9.9977E-06	1.7358E-04	4.2211E-05	-6.83E-02	1.59E+01	2.94E-01	0.078	0.775	-0.010

7	0.122173048	-1.6020E-05	2.0174E-04	6.2508E-05	-3.35E-01	1.81E+01	3.17E-01	0.091	0.879	-0.018
8	0.13962634	-1.6708E-05	2.2726E-04	8.9562E-05	-7.03E-01	2.16E+01	4.27E-01	0.113	1.052	-0.002
9	0.157079633	-1.6713E-05	2.5580E-04	1.1802E-04	-1.08E+00	2.57E+01	5.56E-01	0.145	1.250	0.017
10	0.174532925	-2.0093E-05	2.7917E-04	1.2412E-04	-1.11E+00	2.74E+01	5.69E-01	0.179	1.328	0.009
11	0.191986218	-2.1675E-05	2.5693E-04	7.0862E-05	-2.81E-01	2.23E+01	3.63E-01	0.194	1.072	-0.033
12	0.20943951	-2.5136E-05	2.5203E-04	6.7991E-05	-2.69E-01	2.08E+01	2.99E-01	0.199	0.997	-0.047
13	0.226892803	-2.3854E-05	2.4804E-04	5.1387E-05	8.98E-03	1.99E+01	2.64E-01	0.220	0.949	-0.054
14	0.244346095	-1.0674E-05	2.2240E-04	1.5589E-05	5.91E-01	1.91E+01	3.02E-01	0.253	0.897	-0.032
15	0.261799388	-1.2386E-05	2.2975E-04	1.0525E-05	7.01E-01	1.91E+01	2.78E-01	0.274	0.892	-0.042
16	0.27925268	-1.0504E-05	2.2848E-04	1.2825E-05	6.65E-01	1.96E+01	3.08E-01	0.295	0.909	-0.033
17	0.296705973	-1.2757E-05	2.3523E-04	1.2152E-05	6.93E-01	1.96E+01	2.87E-01	0.312	0.906	-0.042
18	0.314159265	-1.5309E-05	2.3942E-04	1.9891E-05	5.63E-01	1.97E+01	2.81E-01	0.324	0.908	-0.046
19	0.331612558	-1.7494E-05	2.4830E-04	1.8370E-05	6.15E-01	1.99E+01	2.63E-01	0.346	0.912	-0.055
20	0.34906585	-1.4275E-05	2.5267E-04	2.1037E-05	6.03E-01	2.13E+01	3.22E-01	0.384	0.968	-0.042

Table A.1 Measured data for a clean ATR-72 wing. Re = $2.005 \cdot 10^5$, $M_\infty = 0.0792$

		Averages of logged samples			**Loads**			**Aerodynamic coefficients**		
α(°)	α(rad)	Chan1 (V/V)	Chan2 (V/V)	Chan3 (V/V)	A (N)	N (N)	M (Nm)	c_d	c_l	c_m
-20	-0.34906585	5.9649E-05	-2.3860E-04	-1.7517E-04	3.00E+00	-1.92E+01	-2.67E-01	0.458	-0.831	0.047
-19	-0.331612558	5.3616E-05	-2.3024E-04	-1.7166E-04	2.84E+00	-1.98E+01	-3.23E-01	0.447	-0.871	0.030
-18	-0.314159265	5.8312E-05	-2.1629E-04	-1.7650E-04	3.11E+00	-1.75E+01	-2.60E-01	0.410	-0.768	0.037
-17	-0.296705973	5.7282E-05	-1.9349E-04	-1.6802E-04	3.08E+00	-1.50E+01	-2.06E-01	0.358	-0.657	0.038
-16	-0.27925268	5.6820E-05	-1.7794E-04	-1.6592E-04	3.13E+00	-1.35E+01	-1.81E-01	0.329	-0.592	0.036
-15	-0.261799388	5.7339E-05	-1.6428E-04	-1.6594E-04	3.22E+00	-1.20E+01	-1.55E-01	0.304	-0.528	0.035
-14	-0.244346095	5.8021E-05	-1.5313E-04	-1.6092E-04	3.22E+00	-1.04E+01	-1.09E-01	0.276	-0.455	0.040
-13	-0.226892803	5.5526E-05	-1.3688E-04	-1.5801E-04	3.20E+00	-9.35E+00	-1.07E-01	0.255	-0.410	0.032
-12	-0.20943951	5.5621E-05	-1.2360E-04	-1.5276E-04	3.20E+00	-7.65E+00	-6.52E-02	0.231	-0.333	0.035
-11	-0.191986218	5.5996E-05	-1.0846E-04	-1.5136E-04	3.27E+00	-5.99E+00	-3.28E-02	0.213	-0.257	0.035
-10	-0.174532925	5.3898E-05	-1.0015E-04	-1.5116E-04	3.26E+00	-5.79E+00	-4.88E-02	0.206	-0.251	0.027
-9	-0.157079633	5.2662E-05	-8.8761E-05	-1.4128E-04	3.14E+00	-4.29E+00	-7.72E-03	0.184	-0.183	0.032
-8	-0.13962634	5.1004E-05	-7.9460E-05	-1.3849E-04	3.10E+00	-3.66E+00	-5.29E-03	0.175	-0.156	0.028
-7	-0.122173048	5.0396E-05	-6.7024E-05	-1.2965E-04	3.01E+00	-1.97E+00	4.14E-02	0.158	-0.078	0.033
-6	-0.104719755	4.6983E-05	-5.7988E-05	-1.2842E-04	2.96E+00	-1.99E+00	1.30E-02	0.154	-0.082	0.021
-5	-0.087266463	4.6775E-05	-5.4435E-05	-1.1775E-04	2.80E+00	-8.90E-01	6.03E-02	0.140	-0.031	0.032
-4	-0.06981317	4.4407E-05	-4.8798E-05	-1.1253E-04	2.69E+00	-6.28E-01	5.82E-02	0.133	-0.021	0.029
-3.5	-0.061086524	4.6501E-05	-5.1392E-05	-1.0881E-04	2.66E+00	1.15E-02	9.86E-02	0.130	0.009	0.040
-3	-0.052359878	4.4703E-05	-4.9132E-05	-1.0434E-04	2.56E+00	5.76E-02	9.63E-02	0.125	0.009	0.039
-2.5	-0.043633231	4.2966E-05	-4.7544E-05	-1.0035E-04	2.46E+00	1.96E-02	9.18E-02	0.120	0.006	0.037
-2	-0.034906585	3.6226E-05	-4.3832E-05	-9.8235E-05	2.28E+00	-1.39E+00	1.46E-02	0.114	-0.064	0.017
-1.5	-0.026179939	3.6920E-05	-4.1682E-05	-9.3511E-05	2.23E+00	-6.24E-01	4.70E-02	0.110	-0.028	0.024
-1	-0.017453293	3.2910E-05	-3.7752E-05	-8.9248E-05	2.08E+00	-1.07E+00	1.61E-02	0.103	-0.050	0.015
-0.5	-0.008726646	3.1053E-05	-3.4576E-05	-8.3359E-05	1.95E+00	-8.43E-01	2.03E-02	0.096	-0.040	0.015

0	0	2.5441E-05	-2.4535E-05	-7.5973E-05	1.75E+00	-9.23E-01	-1.05E-02	0.086	-0.045	0.003
0.5	0.008726646	2.3760E-05	-1.5694E-05	-7.1540E-05	1.69E+00	-2.20E-01	-2.10E-03	0.082	-0.011	0.001
1	0.017453293	2.0054E-05	-8.3251E-06	-6.4019E-05	1.51E+00	2.34E-03	-1.02E-02	0.074	-0.001	-0.004
1.5	0.026179939	1.7729E-05	4.9301E-07	-5.7726E-05	1.40E+00	6.62E-01	-2.73E-03	0.069	0.031	-0.006
2	0.034906585	1.3897E-05	1.6242E-05	-4.6778E-05	1.22E+00	1.91E+00	1.38E-02	0.063	0.091	-0.010
2.5	0.043633231	1.0369E-05	2.2974E-05	-4.9395E-05	1.21E+00	1.34E+00	-3.57E-02	0.062	0.063	-0.025
3	0.052359878	1.0102E-05	3.9241E-05	-3.8835E-05	1.12E+00	3.63E+00	2.83E-02	0.064	0.174	-0.018
3.5	0.061086524	1.1605E-05	4.9263E-05	-3.7109E-05	1.19E+00	5.15E+00	7.01E-02	0.074	0.247	-0.013
4	0.06981317	1.3357E-05	7.0540E-05	-3.2149E-05	1.28E+00	8.06E+00	1.45E-01	0.090	0.388	-0.006
5	0.087266463	8.3151E-06	8.7056E-05	-1.9836E-05	1.05E+00	9.14E+00	1.52E-01	0.090	0.440	-0.012
6	0.104719755	9.6981E-06	1.1992E-04	7.3451E-06	8.22E-01	1.48E+01	3.32E-01	0.115	0.713	0.015
7	0.122173048	9.4599E-06	1.3945E-04	4.1802E-06	9.83E-01	1.63E+01	3.43E-01	0.145	0.785	0.007
8	0.13962634	8.7502E-06	1.6506E-04	1.1235E-05	9.98E-01	1.91E+01	3.99E-01	0.178	0.917	0.007
9	0.157079633	4.0569E-06	1.9332E-04	1.9231E-05	9.14E-01	2.11E+01	4.09E-01	0.205	1.009	-0.004
10	0.174532925	1.3618E-05	2.0860E-04	-7.5932E-06	1.69E+00	2.32E+01	4.47E-01	0.278	1.101	-0.006
11	0.191986218	7.7985E-06	2.0189E-04	-3.7530E-05	2.00E+00	1.86E+01	2.32E-01	0.269	0.872	-0.056
12	0.20943951	8.5057E-06	1.9073E-04	-5.4236E-05	2.22E+00	1.64E+01	1.55E-01	0.273	0.762	-0.070
13	0.226892803	1.0232E-05	1.8995E-04	-6.0433E-05	2.37E+00	1.63E+01	1.51E-01	0.292	0.752	-0.071
14	0.244346095	8.4030E-06	1.8839E-04	-6.3639E-05	2.36E+00	1.54E+01	1.11E-01	0.294	0.704	-0.080
15	0.261799388	1.0381E-05	1.9045E-04	-6.6243E-05	2.47E+00	1.60E+01	1.29E-01	0.319	0.723	-0.077
16	0.27925268	1.1525E-05	1.9629E-04	-6.6615E-05	2.54E+00	1.68E+01	1.52E-01	0.346	0.757	-0.075
17	0.296705973	1.2128E-05	2.0350E-04	-6.3310E-05	2.54E+00	1.80E+01	1.84E-01	0.375	0.803	-0.071
18	0.314159265	1.2995E-05	2.1245E-04	-6.0252E-05	2.56E+00	1.93E+01	2.21E-01	0.411	0.858	-0.066
19	0.331612558	1.5729E-05	2.2814E-04	-5.8600E-05	2.70E+00	2.17E+01	2.87E-01	0.470	0.960	-0.059
20	0.34906585	1.2892E-05	2.3717E-04	-4.8664E-05	2.51E+00	2.25E+01	3.04E-01	0.492	0.992	-0.059

Table A.2 Measured data for an ATR-72 wing with icing. Re = $2.005 \cdot 10^5$, $M_\infty = 0.0792$